

kinetic states (Zagotta et al., 1994). The large number derives partly from independent transitions in the four subunits that form the channel. Although rhodopsin does not consist of subunits, it does contain seven transmembrane helices and four cytoplasmic loops, which are thought to change position after photoisomerization (Farahbakhsh et al., 1995; Altenbach et al., 1996). States of different catalytic activity could conceivably be produced by relative movements of these structures.

Functional role of reproducibility

What biological purpose might be served by reproducible elementary responses? A possible answer is that reproducibility allows the rod to encode the number of active rhodopsin molecules and thus allows accurate estimation of light intensity. However, the accuracy with which the intensity can be estimated will be limited by Poisson fluctuations in the number of photoisomerizations as well as noise intrinsic to the rod, and for all but the dimmest lights Poisson fluctuations dominate. Most of the rod's dark noise is due to thermal isomerization of rhodopsin, which occurs about once every 30 s in a toad rod (Baylor et al., 1980). The requirement that the number of photoisomerizations significantly exceed this number apparently sets the ultimate limit to the sensitivity of rod vision (Aho et al., 1988). The noise variance arising from fluctuations in the elementary response is 20–25 times smaller than that due to Poisson fluctuations. Thus the reproducibility of the elementary response allows the rod to encode the difference between five and six photoisomerizations, whereas Poisson fluctuations in the number of absorbed photons make this difference minimally informative about real differences in light intensity. The elementary response seems "overengineered" for simply estimating light intensity.

Alternatively, reproducibility might preserve information about the times at which photons are absorbed. In a noiseless rod with identical elementary responses, the times of photon absorption could be recovered by unfolding the time course of the elementary response from the observed membrane current. In the real rod, two factors will limit the accuracy of the recovery: fluctuations in the shape of the elementary response (Baylor et al., 1979b) and continuous noise in the transduction cascade (Baylor et al., 1980; Rieke and Baylor, 1996). The contribution of fluctuations in the shape of the elementary response was assessed in the following way. Elementary responses and failures were isolated from an amplitude histogram such as that in Fig. 4. The most likely time of photoisomerization was then estimated from each elementary response by two steps (see Fig. 19, A and B): 1) the probability of photoisomerization as a function of time was calculated by operating on the photocurrent with a matched filter calculated from the rod's elementary response and continuous dark noise spectrum (Bialek and Owen, 1990); 2) the peak of the time-dependent probability was taken as an estimate of the time of photo-

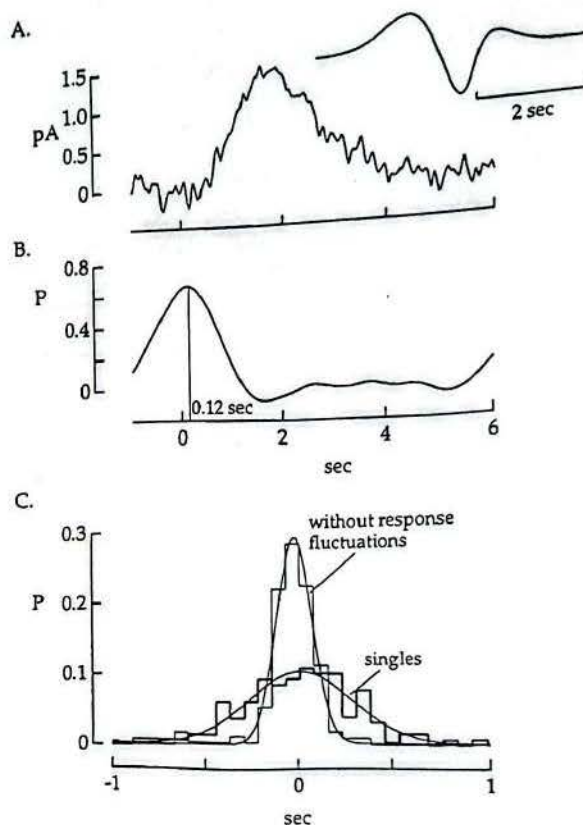


FIGURE 19 The contribution of elementary response fluctuations to the precision of estimated photoisomerization times. (A) Response to a single photoisomerization at time $t = 0$ from the experiment of Fig. 3. The time of photoisomerization was estimated from the photocurrent by correcting for the impulse response of the transduction cascade. Without noise it would be possible to recover the time of photoisomerization exactly, but noise introduces some temporal imprecision. The inset shows the impulse response of a filter that takes as input the rod current and produces an estimate of the probability of photoisomerization as a function of time. The filter chosen provides the best estimate of the time-dependent probability of photoisomerization given the single photon response and dark noise (see Bialek and Owen, 1990). The filter utilizes the entire rod response and thus introduces a delay of 6 s in the estimate. (B) Time-dependent probability of photoisomerization calculated from single photon response and filter in A. The 6-s delay has been removed to facilitate comparison with the actual time of photoisomerization of $t = 0$. The estimated time of photoisomerization was taken as the peak of the time-dependent probability (vertical line), which occurred at $t = 0.12$ s in this case. (C) Probability densities of estimated times of photoisomerization calculated as in A and B. The thick trace represents estimates from 129 single photon responses. The Gaussian fitted to the distribution has a standard deviation of 226 ms. Continuous noise and fluctuations in the elementary response contribute to the width of this distribution. The thin trace represents estimates from 223 failures, each with an added stereotyped response (the average of the singles). The Gaussian fitted to this distribution has a standard deviation of 95 ms. This distribution reflects timing errors introduced by continuous noise alone. Comparison of the two distributions indicates that fluctuations in the shape of the elementary response limit the temporal precision of the estimated photon times.

isomerization. As the entire rod response was used to make the estimate, the procedure introduced a delay equal to the duration of the elementary response.

The distribution of estimated photoisomerization times relative to the actual time is shown in Fig. 19 C (thick

trace), where it is fitted by a Gaussian of standard deviation 275 ms. In results from eight cells the mean standard deviation was 252 ms, so that the imprecision of the time estimate was considerably smaller than the duration of the elementary response. Both response fluctuations and continuous noise contribute to the scatter in the time estimate. To estimate the contribution of continuous noise alone, a stereotyped single photon response was added to the current from each trial in which no photoisomerization occurred and the estimation procedure was repeated. The distribution of these estimated times is shown by the thin trace in Fig. 19 C, where it is fitted by a Gaussian of standard deviation 95 ms. In eight cells the mean standard deviation was 118 ms, considerably smaller than the estimate of 252 ms from the actual elementary responses. The conclusion is that fluctuations in the shape of the elementary response limit the precision with which photoisomerization times can be estimated.

The analysis above indicates that the temporal precision of operations in the rod pathways would suffer if reproducibility of the elementary response failed. This temporal precision may be critical for tasks such as correctly identifying the direction of motion of a visual stimulus or correctly identifying an object that suddenly appears in the visual field.

We thank Drs. E. J. Chichilnisky, B. Hille, and M. Meister for careful reading of the manuscript; W. Bialek, Y. Koutalos, and L. Stryer for stimulating discussions; and Robert Schneeveis for excellent technical assistance.

This work was supported by the National Eye Institute through grants EY01543 (to DAB) and EY11850 (to FR).

REFERENCES

- Aho, A.-C., K. Donner, C. Hydén, L. O. Larsen, and T. Reuter. 1988. Low retinal noise in animals with low body temperature allows high visual sensitivity. *Nature*. 334:348–350.
- Altenbach, C., K. Yang, D. L. Farrens, Z. T. Farahbakhsh, H. G. Khorana, and W. L. Hubbell. 1996. Structural features and light-dependent changes in the cytoplasmic interhelical E-F loop region of rhodopsin: a site-directed spin-labeling study. *Biochemistry*. 35:12470–12478.
- Arshavsky, V. Yu., and M. D. Bownds. 1992. Regulation of deactivation of photoreceptor G protein by its target enzyme and cGMP. *Nature*. 357: 416–417.
- Baylor, D. A., T. D. Lamb, and K.-W. Yau. 1979a. The membrane current of single rod outer segments. *J. Physiol. (Lond.)*. 288:589–611.
- Baylor, D. A., T. D. Lamb, and K.-W. Yau. 1979b. Responses of retinal rods to single photons. *J. Physiol. (Lond.)*. 288:613–634.
- Baylor, D. A., G. Matthews, and K.-W. Yau. 1980. Two components of electrical dark noise in toad retinal rod outer segments. *J. Physiol. (Lond.)*. 309:591–621.
- Baylor, D. A., B. J. Nunn, and J. L. Schnapf. 1984. The photocurrent, noise and spectral sensitivity of rods of the monkey *Macaca fascicularis*. *J. Physiol. (Lond.)*. 357:575–607.
- Bennett, N., and A. Sitaramayya. 1988. Inactivation of photoexcited rhodopsin in retinal rods: the roles of rhodopsin kinase and 48-kDa protein (arrestin). *Biochemistry*. 27:1710–1715.
- Bialek, W., and W. G. Owen. 1990. Temporal filtering in retinal bipolar cells: elements of an optimal computation? *Biophys. J.* 58:1227–1233.
- Cervetto, L., L. Lagnado, R. J. Perry, D. W. Robinson, and P. A. McNaughton. 1989. Extrusion of calcium from rod outer segments is driven by both sodium and potassium gradients. *Nature*. 337:740–743.
- Chen, J., C. L. Makino, N. S. Peachey, D. A. Baylor, and M. I. Simon. 1995. Mechanisms of rhodopsin inactivation *in vivo* as revealed by a COOH-terminal truncation mutant. *Science*. 267:374–377.
- Corson, D. W., M. C. Cornwall, and D. R. Pepperberg. 1994. Evidence for the prolonged photoactivated lifetime of an analogue visual pigment containing 11-cis-9-desmethylretinal. *Vis. Neurosci.* 11:91–98.
- Erickson, M. A., L. Lagnado, S. Zozulya, T. A. Neubert, L. Stryer, and D. A. Baylor. 1998. The effect of recombinant recoverin on the photoresponse of truncated rod photoreceptors. *Proc. Natl. Acad. Sci. USA*. 95:6474–6479.
- Farahbakhsh, Z. T., K. D. Ridge, H. G. Khorana, and W. L. Hubbell. 1995. Mapping light-dependent structural changes in the cytoplasmic loop connecting helices C and D in rhodopsin: a site-directed spin labeling study. *Biochemistry*. 34:8812–8819.
- Fung, B. K. 1983. Characterization of transducin from bovine retinal rod outer segments. I. Separation and reconstitution of the subunits. *J. Biol. Chem.* 258:10495–10502.
- Gray-Keller, M. P., and P. B. Detwiler. 1994. The calcium feedback signal in the phototransduction cascade of vertebrate rods. *Neuron*. 13: 849–861.
- Hecht, S., S. Shlaer, and M. Pirenne. 1942. Energy, quanta and vision. *J. Gen. Physiol.* 25:819–840.
- Karpen, J. W., A. L. Zimmerman, L. Stryer, and D. A. Baylor. 1988. Gating kinetics of the cyclic-GMP-activated channel of retinal rods: flash photolysis and voltage-jump studies. *Proc. Natl. Acad. Sci. USA*. 85:1287–1291.
- Kawamura, S. 1993. Rhodopsin phosphorylation as a mechanism of cyclic GMP phosphodiesterase regulation by S-modulin. *Nature*. 362: 855–857.
- Koch, K. W., and L. Stryer. 1988. Highly cooperative feedback control of retinal rod guanylate cyclase by calcium ions. *Nature*. 334:64–66.
- Koutalos, Y., K. Nakatani, T. Tamura, and K.-W. Yau. 1995a. Characterization of guanylate cyclase activity in single retinal rod outer segments. *J. Gen. Physiol.* 106:863–890.
- Koutalos, Y., K. Nakatani, and K.-W. Yau. 1995b. The cGMP-phosphodiesterase and its contribution to sensitivity regulation in retinal rods. *J. Gen. Physiol.* 106:891–921.
- Koutalos, Y., and K.-W. Yau. 1996. Regulation of sensitivity in vertebrate rod photoreceptors by calcium. *Trends Neurosci.* 19:73–81.
- Krupnick, J. G., V. V. Gurevich, and J. L. Benovic. 1997. Mechanism of quenching of phototransduction. Binding competition between arrestin and transducin for phosphorhodopsin. *J. Biol. Chem.* 272:18125–18131.
- Lagnado, L., and D. A. Baylor. 1992. Signal flow in visual transduction. *Neuron*. 8:995–1002.
- Lagnado, L., and D. A. Baylor. 1994. Calcium controls light-triggered formation of catalytically active rhodopsin. *Nature*. 367:273–277.
- Langlois, G., C. K. Chen, K. Palczewski, J. B. Hurley, and T. M. Vuong. 1996. Responses of the phototransduction cascade to dim light. *Proc. Natl. Acad. Sci. USA*. 93:4677–4682.
- Lybarsky, A., S. Nikanov, and E. N. Pugh. 1996. The kinetics of inactivation of the rod phototransduction cascade with constant Ca^{2+} . *J. Gen. Physiol.* 107:19–34.
- Matthews, H. R., R. L. W. Murphy, G. L. Fain, and T. D. Lamb. 1988. Photoreceptor light adaptation is mediated by cytoplasmic calcium concentration. *Nature*. 334:67–69.
- McCarthy, S. T., J. P. Younger, and W. G. Owen. 1996. Dynamic spatially non-uniform calcium regulation in frog rods exposed to light. *J. Neurophysiol.* 76:1991–2004.
- Miller, J. L., and E. A. Dratz. 1984. Phosphorylation at sites near rhodopsin's carboxyl-terminus regulates light initiated cGMP hydrolysis. *Vision Res.* 24:1509–1521.
- Murnick, J. G., and T. D. Lamb. 1996. Kinetics of desensitization induced by saturating flashes in toad and salamander rods. *J. Physiol. (Lond.)*. 495:1–13.
- Nakatani, K., and K.-W. Yau. 1988a. Calcium and light adaptation in retinal rods and cones. *Nature*. 334:69–71.

G-Protein-Coupled Enzyme Cascades Have Intrinsic Properties that Improve Signal Localization and Fidelity

Fidelidad? ↗ precision?

Sharad Ramanathan,* Peter B. Detwiler,† Anirvan M. Sengupta,‡ and Boris I. Shraiman[†]

*Bell Labs, Lucent Technologies, Murray Hill, New Jersey; †Dept of Physiology and Biophysics, University of Washington, Seattle, Washington; and ‡Department of Physics and the BioMaPS Institute, Rutgers University, Piscataway, New Jersey

ABSTRACT G-protein-coupled enzyme cascades are used by eukaryotic cells to detect external signals and transduce them into intracellular messages that contain biological information relevant to the cell's function. Since G-protein-coupled receptors that are designed to detect different kinds of external signals can generate the same kind of intracellular response, effective signaling requires that there are mechanisms to increase signal specificity and fidelity. Here we examine the kinetic equations for the initial three stages in a generic G-protein-coupled cascade and show that the physical properties of the transduction pathway result in two intrinsic features that benefit signaling. 1), The response to a single activated receptor is naturally confined to a localized spatial domain, which could improve signal specificity by reducing cross talk. 2), The peak of the response generated by such a signaling domain is limited. This saturation effect reduces trial-to-trial variability and increases signaling fidelity by limiting the response to receptors that remain active for longer than average. We suggest that this mechanism for reducing response fluctuations may be a contributing factor in making the single photon responses of vertebrate retinal rods so remarkably reproducible.

INTRODUCTION

The functional viability of multicellular organisms depends on their constituent cellular building blocks being able to communicate with each other. This requires that cells have a way to detect and respond specifically to select external signals. One of the most common strategies for doing this makes use of a three-stage G-protein-coupled enzyme cascade (Lodish et al., 2000). In the first stage, a specialized membrane receptor protein, R , is activated by its interaction with a specific external signal, such as by binding a particular ligand or absorbing a photon of a particular wavelength. In the second stage, the activated receptor, R^* , turns on a heterotrimeric G-protein, G^* , by catalyzing GDP/GTP exchange on the α -subunit of the protein. During the time it stays active, t_R , a single R^* will serially excite many G-proteins and thus amplify the original signal, i.e., one R^* to many G^* . In the third stage, each G^* associates with an effector protein, E , forming a G^*-E complex that stimulates the effector. We shall refer to the G^*-E complex as the active effector, E^* . Activated effector proteins are most commonly enzymes that control the level of an intracellular second messenger such as a cyclic nucleotide or Ca^{2+} . The resulting change in second messenger concentration represents the output signal of the transduction process and is further amplified by each activated enzyme, E^* , which turns over more than one substrate molecule.

The strength of the cascade's output signal, i.e., the size of the change in second messenger concentration, depends on how many effector enzymes are active and how long they

stay active. Thus the overall gain of the cascade depends on the rate of its inactivation. This involves shutting off the two catalytically active intermediates, R^* and E^* . The life of the activated receptor, R^* , and the steady production of G^* it catalyzes, are terminated after receptor phosphorylation. The catalytic activity of E^* is terminated when the GTPase activity of G^* within the G^*-E complex hydrolyzes GTP to GDP, leading to the dissociation of the complex and the shutting off of effector activity. The G-protein, in its inactive (GDP-bound) state is no longer able to excite the effector and E^* returns to its resting state. Additional elements, which control both R^* shutoff and the intrinsic activity of G-protein GTPase (Berman and Gilman, 1998; He et al., 1998; Makino et al., 1999; Arshavsky et al., 2002) provide a mechanism for gain control. Our treatment of the G-protein cascade considers the pathway only so far as the activation of effector enzyme; it does not include the dynamics of the second messenger signal.

The activated elements of the cascade (R^* , G^* , and E^*) that ultimately generate the second messenger signal are all membrane-associated and diffuse two-dimensionally on the membrane surface. Here we consider two inherent properties of signals that arise as a consequence of being generated by an amplified enzyme cascade that is confined to the membrane. By examining the first steps of G-protein signaling that follow the excitation of a single receptor we show that the resulting activity of the effector enzyme is naturally localized to a small $\sim 1 \mu\text{m}$ radius response domain and the peak amplitude of the response is limited. Both of these built-in effects would serve to benefit the signaling process. The establishment of a localized signaling domain would reduce cross talk and improve signal specificity. Limiting the peak amplitude of the response would decrease

Submitted December 30, 2003, and accepted for publication October 8, 2004.

Address reprint requests to Boris I. Shraiman at his current address, Kavli Institute for Theoretical Physics, University of California, Santa Barbara, CA 93016. Tel.: 805-893-2835; E-mail: shraiman@kitp.ucsb.edu.

© 2005 by the Biophysical Society

0006-3495/05/05/3063/09 \$2.00

doi: 10.1529/biophysj.103.039321

trial-to-trial variability and thus increase response reproducibility and signal fidelity.

Our analysis is relevant to membrane-localized enzyme cascades in general, but our treatment is guided specifically by the phototransduction process in vertebrate retinal rods. We have chosen this as our model because it is the most thoroughly studied and best-understood example of G-protein-coupled signaling (Stryer, 1991; Baylor, 1996). The basic scheme is the same as the generic one described above. An external signal (a visible photon) activates a membrane receptor (rhodopsin, *Rh*). The light-activated receptor (*Rh*^{*}) serially activates many G-proteins (also known as transducin, or *T*) molecules. The activated transducin (*T*^{*}) stimulate one-to-one an equal number of effector enzymes (phosphodiesterase; i.e., PDE). The activated phosphodiesterase (PDE^{*}) hydrolyzes cyclic nucleotides (cyclic GMP; i.e., cGMP), generating an amplified second messenger signal consisting of a fall in the resting level of cGMP. In retinal rods the drop in cGMP closes ion channels that are opened by binding cGMP (cyclic nucleotide-gated channels). This reduces the standing inward cationic current that circulates through the rod in darkness and completes the phototransduction process that converts light into an amplified electrical signal, a change in cell membrane potential.

Another reason we have focused our attention on phototransduction is that our analysis considers the events that follow the activation of a single receptor molecule. Detailed information about the signal that G-protein-coupled cascades produce in response to a single activated receptor molecule is only available for photoreceptors, which produce a robust response to the absorption of a single photon (Baylor, 1984).

The G-protein module

The analysis begins by considering the rate equations that describe the localized activation and deactivation of G-protein and effector enzyme caused by activated receptor *R*^{*}:

$$\frac{d[G^*]}{dt} = k_1[R^*] - k_2[E][G^*] + D_G \nabla^2 [G^*], \quad (1)$$

$$\frac{d[E^*]}{dt} = k_2[E][G^*] - k_H[E^*] + D_E \nabla^2 [E^*]. \quad (2)$$

In addition to formation and destruction of active species these equations describe their diffusion on the membrane, away from their sites of production. The G-protein and effector enzyme are membrane-associated proteins and their concentrations are expressed as areal densities (number per μm^2) denoted by the bracket [...]. Their diffusion coefficients D_G and D_E are reported (Pugh and Lamb, 1993; Lamb, 1994) to have similar values in the 1–2 $\mu\text{m}^2/\text{s}$ range. The constant k_1 is the rate of activation of G^* by R^* . More generally this process obeys Michaelis-Menten kinetics, $k_1[R^*]/(1+K_m/[G])$, which we assume operates in the

saturation limit when $[G] \gg K_m$, as is apparently the case for phototransduction. The kinetic constant k_2 , describes the formation of the G^*-E complex and thus the production of E^* . The rate of E^* decay is governed by k_H , the rate of G^* inactivation due to GTP hydrolysis by the G-protein's GTPase activity within the G^*-E complex. We assume that E and E^* have the same diffusivity (D_E). As a result, the total E concentration, $[E_{\text{tot}}] = [E] + [E^*]$, satisfies a simple diffusion equation, and is taken to be a constant in this study.

The kinetic equations (Eqs. 1 and 2) do not describe the full G-protein cycle, nor do they consider the possible dissociation of G^* from the membrane, which might become important under conditions of prolonged strong excitation (Chabre and Deterre, 1989; Heck and Hofmann, 1993, 2001). Nevertheless, they can be used to describe the response evoked by the activation of a single receptor molecule. In the continuum kinetic equation description employed here, single receptor activation is represented as a density of active receptor, $[R^*] = A(t)\delta(r-r^*)$, sharply peaked at the location, r^* , of the active receptor molecule and non-zero only over the time interval $0 < t < t_R$, where t_R denotes the shutoff time of the activated receptor (note $A(t) = 1$ for $0 < t < t_R$). The shutoff of the active receptor is a random variable with an average lifetime, τ_R , which is controlled by the rate of receptor phosphorylation and arrestin binding (Chabre and Deterre, 1989; Stryer, 1991; Helmreich and Hofmann, 1995). The difference between t_R (the shutoff time of a single activated receptor for a single trial) and lifetime τ_R (defined as the average t_R taken over many trials) is important, and will come up later in the analysis.

Note that this description does not prevent the incorporation of other general properties of G-protein signaling. For example, multistep deactivation of R^* may be accommodated by endowing t_R with an appropriate sub-Poisson statistical distribution, whereas the diffusion of R^* may be represented by making the locus of activity, r^* , follow a random trajectory and averaging E^* activation patterns over all possible trajectories.

Localization of G-protein signaling

Let us consider a response defined as the effector activity generated by a single catalytically active receptor molecule acting as a point source of $[G^*]$. The details of the analysis can be found in the Appendix. In the text we describe the physical mechanism of signal localization and saturation and then describe the relationships between particular parameters and the properties of the localization and saturation process. A full quantitative description obtained by the numerical solution of Eqs. 1 and 2, as described in the Appendix, is presented in the figures. To simplify the discussion we shall presently ignore effector diffusion, for it does not affect the key aspects of the mechanism.

Free G^* will spread spatially from its site of production with a characteristic length, l_d , that represents a competition

between its outward diffusion and its sequestration, upon binding with free E , into a G^* - E complex. This length can be expressed as

$$l_d = \sqrt{\frac{D_G}{k_2 [E]}} \quad (3)$$

and is quite short (<100 nm using the parameters in Table 1, and assuming that free effector concentration is of the order of total effector concentration $[E_{tot}]$.) The one-to-one association of G^* and E to produce E^* , reduces free $[E]$.

The resulting initial response domain will have different properties depending on whether the rate of G^* activation is large or small compared to the rate of E^* (i.e., G^* - E complex) deactivation. If the recovery of free E , which follows GTP hydrolysis within the complex, is faster than the rate of G^* production, then there will always be free E on hand to bind to free G^* and prevent its outward spread. For this to happen k_1 must be less than the maximum rate of E recovery within the activated area (πl_d^2), which we estimate as $\pi l_d^2 [E^*] k_H = (\pi D_G k_H / k_2)([E^*]/[E])$ —note that, in the subsaturated condition, $[E^*] < [E]$). Thus a single molecule of activated receptor (R^*) will give rise to a spatially localized subsaturated response domain when $k_1 < (\pi D_G k_H / k_2)([E^*]/[E]) < \pi D_G k_H / k_2$. It is convenient to define a saturation parameter (S) as

$$S = k_1 k_2 / \pi D_G k_H. \quad (4)$$

The subsaturated response domain described above corresponds to $S < 1$. When $S > 1$, the deactivation of E^* , and recovery of free E , is slower than the rate of G^* production. Under these conditions after a time, $t_i \approx \pi l_d^2 [E] / k_1 = \pi D_G / k_2 k_1$ (~3–10 ms for rod phototransduction), nearly all the effector molecules in the initial response domain will be excited, forming an area of saturated activity. This means that if R^* remains active for a time longer than t_i , G^* will no longer be completely absorbed by free E within the l_d region. Molecules of G^* will spill out of the initial response domain and proceed to expand with a radius, r , growing with time as

$$r(t) = \sqrt{\frac{k_1 t}{\pi [E_{tot}]}} \quad (5)$$

TABLE 1 Rod phototransduction parameter values

Description	Value	Reference
D_G	$1.2 \mu\text{m}^2/\text{s}$	Pugh and Lamb (1993)
k_H	10 s^{-1}	Chen et al. (2000)
k_1	$100-1000 \text{ s}^{-1}$	Pugh and Lamb (1993); Kahlert and Hofmann (1991); Leskov et al. (2000)
k_2	$1 \mu\text{m}^2/\text{s}$	Pugh and Lamb (1993)
[Rhodopsin]	$25,000 \mu\text{m}^{-2}$	Hamm and Bownds (1986)
[Transducin]	$2500 \mu\text{m}^{-2}$	Pugh and Lamb (1993)
[Phosphodiesterase]	$200 \mu\text{m}^{-2}$	Dumke et al. (1994)

so that the total number of activated effectors, E^* , will increase as $k_1 t$. This process is illustrated in Fig. 1. The expansion of the response domain continues until it reaches a maximum radius, r_{max} , which is on the order of $\sqrt{k_1 / \pi k_H [E_{tot}]}$. We refer to this process as *spot formation*. It develops with a characteristic time, t_s , which is on the order of $1/k_H$. The internal consistency of this argument requires that the time for spot formation, t_s , be longer than the time it takes for G^* to spread by free diffusion over a distance on the same scale as r_{max} . This time is $\sim r_{max}^2 / 4D_G$, provided $r_{max}^2 k_H / 4D_G = k_1 / 4\pi D_G [E_{tot}] < 1$. This condition is satisfied for the rod parameters in Table 1.

Fig. 2 shows the space and time evolution of the effector response triggered by a single active receptor molecule. The traces present the results of the numerical solution of Eqs. 1 and 2 for $S > 1$. They show snapshots of the spatial profile of the response at different times. As time increases, the response (the spatial distribution of $[E^*]$) converges to a stationary profile and does not change further with time. This illustrates the process of spot formation discussed above and shows that the limiting profile of the response is a saturated area of effector activity. Total effector activation in the case of continuous receptor activity is shown as a function of time in Fig. 3. As the saturated spot forms, the total number of active effectors E^* approaches a limit (Fig. 3 a) equal to k_1 / k_H — a result derived in the Appendix. Fig. 3, b and c, compare the effect for two different values of k_1 and three different values of k_H . In these figures the active effector number is normalized to the amplitude of the saturated response (k_1 / k_H) and time is measured in the units

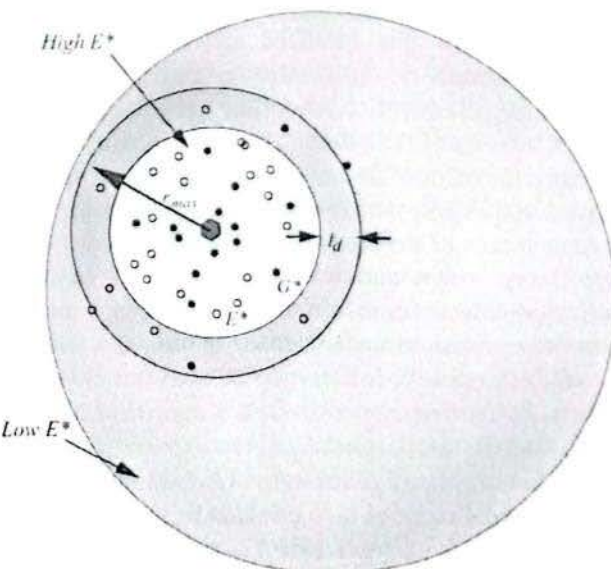


FIGURE 1 Localization of G-protein and effector activation. Hexagon represents location of single active receptor molecule, which activates G-proteins. Active G-protein (solid circles) diffuses outward, binds to the effector and activates it (open circles). Green denotes the activation front which moves out with time and if receptor activity persists, eventually converging to the stationary active spot boundary. See text for details.

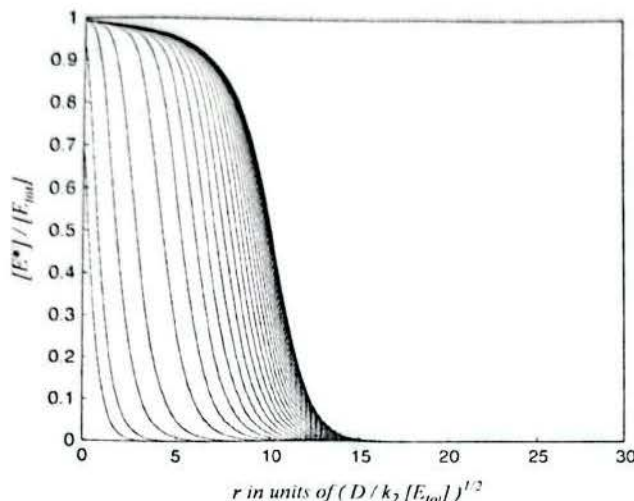


FIGURE 2 The fraction of activated effector is shown as a function of the distance from the excited receptor molecule at various times. The outermost curve corresponds to the saturated spot profile corresponding to stationary response to continuous receptor activity, and the inner curves represent the snapshots of the profile at earlier times, as this stationary profile is approached. Snapshots are taken at $t = 0.015, 0.02, 0.025, 0.05, 0.1, 0.15, 0.2, 0.25, \dots, 3.0$ in units of $1/k_H$. Parameters are $k_H = 3 \text{ s}^{-1}$, $k_1 = 10^4 \text{ s}^{-1}$, and $k_2 = D_G = 1 \mu\text{m}^2/\text{s}$; the total effector density is $[E_{\text{tot}}] = 200 \mu\text{m}^{-2}$.

of $1/k_H$. Normalizing the response and time axes in this way shows that the characteristic time of saturation, t_S , (defined quantitatively as the time for half-maximum effector activation), scales with (and is approximately equal to) k_H^{-1} , with only a weak dependence on k_1 . The maximal active domain size, r_{\max} , as a function of k_H , is shown in Fig. 4. Spot size scales as $\sqrt{k_1/k_H}$.

The effect of this localized saturation on the actual response depends on the duration of receptor activity. The plots in Fig. 3, *b* and *c*, show the growth of normalized effector activity ($E^*(t)$) in response to a maintained step of receptor activation. The effector response to a pulse of receptor activity staying on for time t_R , would depart from the time course of the response to a step, only after receptor shutoff at t_R — at which time the growth of E^* would slow, reach a peak and begin to decline as recovery took over. Hence, the peak amplitude of the response, as a function of time ($E_p^*(t)$), closely follows the behavior of $E^*(t)$. Fig. 5 presents $E_p^*(t)$ determined from the numerical solution of Eqs. 1 and 2, as described in the Appendix. Since the timescale in this figure is in units of $1/k_H$, which, as discussed above, is on the order of t_S , it can also be read as the ratio of t_R to t_S . Thus, for example, when t_R is equal to t_S , the peak amplitude of the response would be ~55% saturated.

Our analysis has, for simplicity's sake, ignored the diffusion of R^* and E^* . These additional diffusive processes are similar in effect to an increase in D_G and lead to the reduction of the saturation parameter S . Yet, since our estimated value of S , based on Table 1 parameters, is in the

range of 10–100 and thus is much larger than 1, its reduction — even by a factor of 2 or 3 — would not take the system out of the $S > 1$ regime analyzed above. Note also that in the regime corresponding to this condition, the size of the spot and the peak amplitude of effector activity are independent of diffusivity and are determined by the balance of k_1 and k_H .

Response fidelity

The output signal of a generic G-protein-coupled enzyme cascade is a change in the level of a soluble second messenger, e.g., a change in cGMP in the case of the retinal rod. The amplitude of the output signal evoked by a single activated receptor depends on how many effector enzymes are activated and how long they stay active. Since the output of an amplified enzymatic cascade is more strongly influenced by changes in upstream events than downstream events, which pass through fewer amplified stages, variations in the amplitude of the output signal would be dominated by noise in the earliest stage of the cascade, i.e., activation of G^* by R^* . The trial-to-trial variation in the signal generated by a single molecule of R^* has only been studied in photoreceptors. This is because the phototransduction cascade is highly amplified and responses evoked by single photon absorptions, i.e., single R^* responses, can be identified and recorded. Rod single photon responses are robust and remarkably reproducible; their mean amplitude is 4–5 times larger than the standard deviation of the fluctuations in their amplitude (Baylor et al., 1979, 1980, 1984; Rieke and Baylor, 1996, 1998; Whitlock and Lamb, 1999; Field and Rieke, 2002; Hamer et al., 2003). The explanation(s) for this exceptionally low variability has not been fully established, but the trial-to-trial variation in the amplitude of the single photon response is recognized to arise predominantly from randomness in shutting off receptor activity. If receptor shutoff were a single-step process occurring at a certain rate, the fluctuations of the shutoff time t_R would have Poisson statistics so that the standard deviation of t_R would be equal to its mean. To suppress noise down to the level observed at the output would require shutoff to be a much less noisy process, which would be the case if it involved multiple steps occurring sequentially with equal rates. If this were the only mechanism for noise suppression in the transduction pathway, 16 R^* shutoff steps would be required for a rod to produce single photon responses with a coefficient of variation, Q — defined as the ratio of the standard deviation to the mean — of 0.25 as observed (number of steps = $(1/Q)^2$) (Rieke and Baylor, 1998).

Another mechanism that would act to reduce response variability and arises as a natural consequence of the properties of a G-protein-coupled enzyme cascade is spot formation, described above. As illustrated in Fig. 2, the effector response to a single R^* converges on a stable response profile which ceases to depend on R^* lifetime. This would reduce the overall variability of the responses by making all the

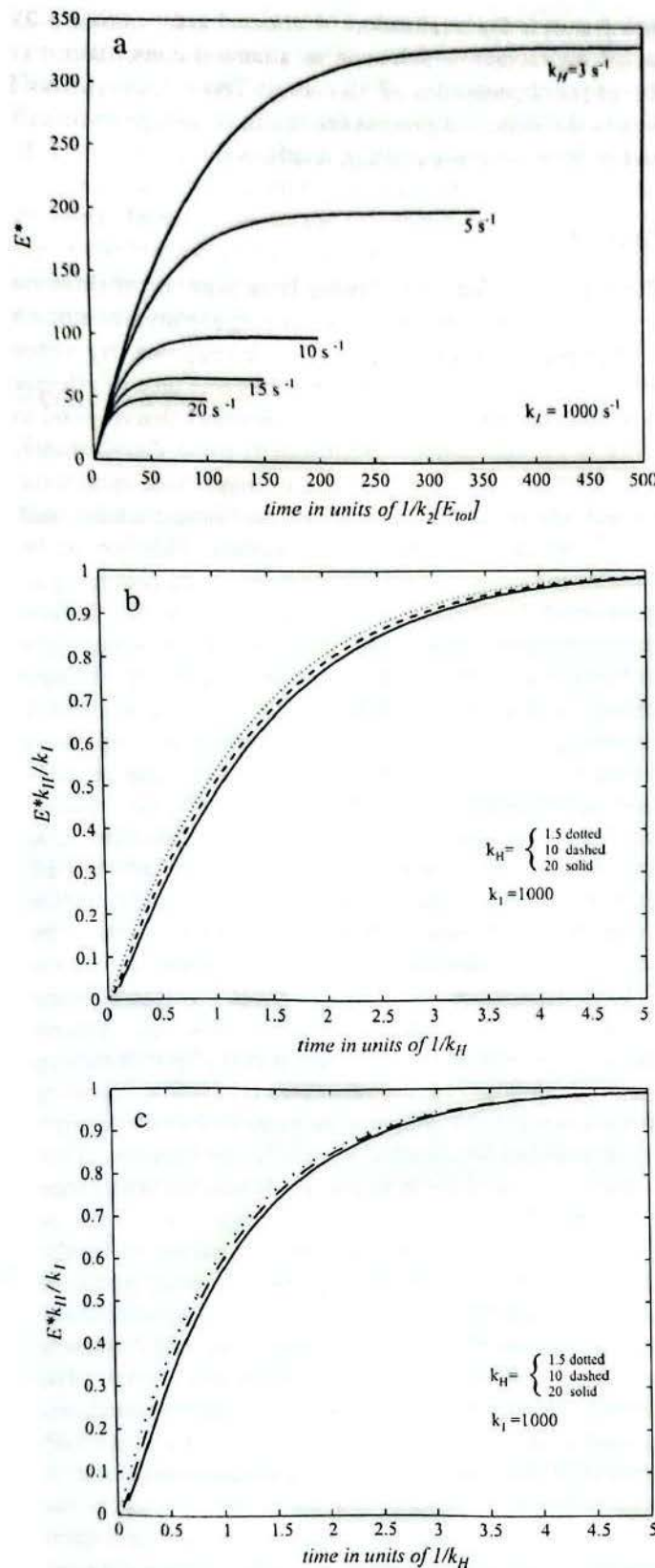


FIGURE 3 (a) Total effector activation as a function of time for a set of different k_H values and fixed $k_1 = 10^3 \text{ s}^{-1}$ (and other parameters the same as in Fig. 2). Maximal activation and the characteristic time of saturation (t_S defined as time corresponding to half-maximal activation) both decrease with increasing k_H . (b) Same as a but with E^* scaled with k_1/k_H and time in units of l/k_H . The fact that they asymptotically approach 1, shows that maximal

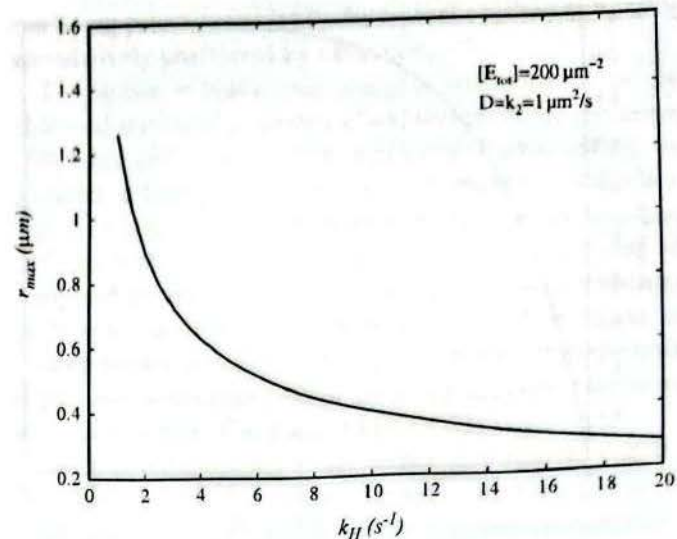


FIGURE 4 Radius of the saturation spot, r_{\max} , as a function of k_H , with $k_1 = 10^3 \text{ s}^{-1}$.

responses evoked by R^* 's that lived longer than a certain time, essentially identical.

In our analysis, response variability was estimated from the dependence of the peak effector response on the shut-off time t_R (see Fig. 5). The coefficient of variation, $Q = \sqrt{\langle E_p^2 \rangle - \langle E_p^* \rangle^2} / \langle E_p^* \rangle$, was used to evaluate response variability, where E_p^* represents the peak effector response. The averaging $\langle \dots \rangle$ is taken over t_R , which is governed by the probability distribution of shutoff times, $P_n(t_R)$, with the average shutoff time $\langle t_R \rangle = \tau_R$,

$$P_n(t_R) = \frac{t_R^{n-1} (n/\tau_R)^n}{(n-1)!} \exp[-nt_R/\tau_R]. \quad (6)$$

This probability distribution corresponds to deactivation via n steps with equal rates n/τ_R and is a generalization of the simple Poisson distribution of shutoff times ($n = 1$). Fig. 6 plots Q for the peak effector response as a function of $\tau_R k_H$ obtained from the numerical solution of Eqs. 1 and 2, as illustrated in Fig. 5. The different curves in Fig. 6 show the decrease in Q , i.e., the decrease in noise, due to spot formation for R^* shutoff with different numbers of shutoff steps. The decrease in variability is due to the sublinearity and saturation of the effector response. The quantitative contribution of this effect is evident from comparing $Q(\tau_R k_H; n)$ with $Q(0; n)$ which corresponds to the limit where response is directly proportional to on-time $E_p^* = k_1 t_R$.

activation is equal to k_1/k_H (as derived in the Appendix). Near-collapse of the curves also shows that the characteristic time of saturation (t_S) scales with $1/k_H$. Furthermore, to the extent that half-activation occurs at $t k_H \approx 1$, we have $t_S \approx k_H$. (c) Same as b, but with $k_1 = 10^2 \text{ s}^{-1}$. Similarity of b and c indicates that the effect of decreasing k_1 is mostly limited to decreasing the total activation level absorbed (in b and c) by rescaling the ordinate (E^*) with k_1/k_H .

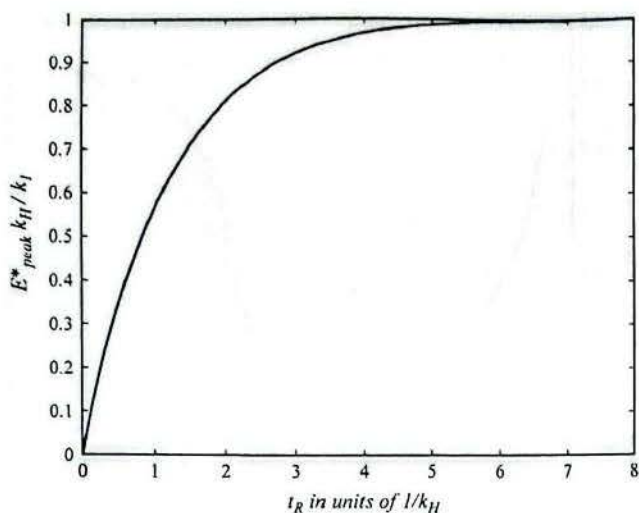


FIGURE 5 Peak effector activation in response to single receptor activity with duration τ_R . The curve is a result of a numerical simulation with the same parameters as in Fig. 2.

DISCUSSION

G-protein-coupled pathways are designed to couple the activation of a surface membrane receptor to the stimulation of an intracellular effector enzyme. We analyzed the kinetic equations (Eqs. 1 and 2) constituting a simplified model for the enzyme cascade that underlies generic G-protein-coupled signaling focusing on the response to single receptor activation. The results show that the three-step cascade has

two features: 1), localization of effector activation and 2), signal saturation—which arise as a natural consequence of the physical properties of signaling. These features could benefit the signaling process by acting to reduce cross talk and increase response fidelity, respectively.

Cross talk

Typical mammalian cells have a large number of different G-protein-coupled receptors that converge to control a much smaller population of different effector enzymes. By virtue of this arrangement it is possible for the same type of effector to be stimulated by different surface receptors that respond to different external signals (Birnbaumer, 1990; Gundermann et al., 1996). In addition, the three principal elements in the cascade (R , G , and E) are all membrane-associated and diffuse two-dimensionally on its surface. This would be expected to further confuse signal specificity by providing an opportunity for diffusion to drive promiscuous interactions between the three components of the cascade, thus making it harder to use a nonspecific change in effector enzyme activity as a message about the detection of a specific external signal. Despite these expected signaling problems, it is well documented that G-protein-coupled signaling pathways are commonly used to produce selective cellular responses to specific stimuli (Gilman, 1987). This shows that there are cell mechanisms to increase signal specificity. One well-recognized mechanism that biology uses to limit the confusion due to cross talk is to physically contain the elements of a cascade that are coupled to a specific receptor. This is done either by fencing them in (by forming a molecular corral made of distinct lipid and protein elements; Okamoto et al., 1998; Fagan et al., 2000; Steinberg and Brunton, 2001) or by tying them up (with scaffolding proteins to tether the components together into a multimolecular transduction complex; Steinberg and Brunton, 2001; Colledge and Scott, 1999; Brady and Limbird, 2002; Albert and Robillard, 2002).

Our analysis shows that in addition to these molecular mechanisms for physical containment, the spatial spread of the effector response of a generic G -protein cascade is self-limiting and naturally forms a restricted signaling domain in the vicinity of the activated membrane receptor. The properties of the localization domain depend essentially on the ratio of the rate of G^* production, k_1 , to the rate of E^* inactivation, k_H , which enters the saturation parameter S (defined by Eq. 4). Saturation parameter S controls the crossover to the saturated spot response, where a local domain of activated effector forms with an area increasing with the time that the receptor has been active until saturating at the maximal radius r_{\max} (given by Eq. 5). Using photoreceptor parameters we estimate the maximum radius of the signaling domain to be $\sim 1 \mu\text{m}$. We note that the size of the signaling domain and the maximal signal amplitude can be controlled by k_1 and k_H parameters and hence by

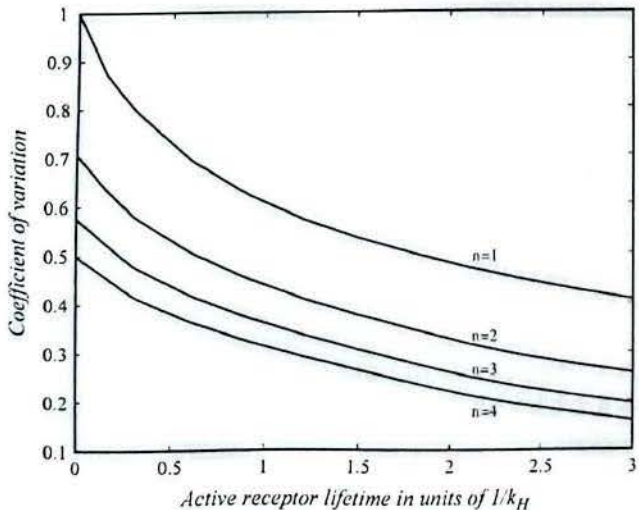


FIGURE 6 Coefficient of variation (ratio of standard deviation to the mean) for peak response as a function of τ_R . Averages are taken in the ensemble of responses with random shutoff times governed by $n = 1, 2, 3, 4$ step Poisson processes with the average shutoff time given by τ_R . Note that with τ_R k_H value of, say, 1.5, there is a significant reduction of the coefficient of variation (denoted by Q in the text) even for $n = 2$. This reduction occurs because the sublinear behavior of the peak response, as a function of the shutoff time (τ_R) (see Fig. 5), reduces the contribution of the events with late receptor shutoff times to the trial-to-trial variability of the responses.

controlling, respectively, the G-protein concentration and the concentration (or activity) of the RGS proteins (Berman and Gilman, 1998; He et al., 1998; Makino et al., 1999; Arshavsky et al., 2002), which modulate the GTPase activity of G^* to influence k_H . These regulatory knobs could provide cells with a mechanism for adapting their response to the stimulus. In any case, to the extent that local signaling domains can reduce cross talk, our analysis shows that cross-talk suppression is an intrinsic feature of the G-protein-coupled enzyme cascade.

Response fidelity

The effector activation process results in a sublinear, saturating dependence of peak effector activity on the on-time of a single R^* so that for long on-times the response becomes independent of the duration of R^* activity. This acts to decrease the fluctuations in peak amplitude that would normally arise from random variation in the shutoff time (t_R) of R^* s and thus serves to increase signal fidelity. This effect, which we have referred to as *spot formation*, may be a contributing factor in the remarkable reproducibility of the single photon response.

Its influence on the trial-to-trial variability of single R^* responses, as measured by the coefficient of variation of the responses, is shown in Fig. 6 for different values of the τ_R . The coefficient of variation of rod single photon responses is ~ 0.25 (Baylor et al., 1979; Rieke and Baylor, 1998; Whitlock and Lamb, 1999; Hamer et al., 2003). Fig. 6 shows that this level of reproducibility can be achieved if the $\tau_R k_H$ is sufficiently large and that the value required for a given Q decreases with increasing number of R^* deactivation steps, n . Thus for $n = 4$, we find that $Q = 0.25$ can be obtained for $\tau_R k_H \approx 2$. On the other hand, looking at Fig. 5 we note that for τ_R this large, typical responses—ones with $t_R \approx \tau_R$ —would have peak response within $\sim 20\%$ of saturation. A somewhat shorter lifetime, such that $\tau_R k_H = 1.5$, would keep the average response further from saturation, yet decrease Q to 0.6 for $n = 1$ and to 0.3 for $n = 4$.

In a previous study Rieke and Baylor (1998) considered the possibility that response saturation suppresses variability and plays a role in the reproducibility of single photon responses. They dismissed this idea, however, by arguing that responses were not saturated because an experimental manipulation that prolonged the lifetime of R^* , i.e., increased τ_R , also increased the peak amplitude of the response. Our results are in fact consistent with this observation, since we see in Fig. 5 that the peak response corresponding to $\tau_R k_H = 1.5$ is well below saturation. The reduction of variability that we are talking about comes from a more subtle effect than outright total effector saturation. The crossover to saturation as a function of the shutoff time selectively suppresses the peaks of the responses evoked by R^* activation events with long on-times. These are the events that correspond to the tail of the t_R distribution, $P(t_R)$, when $t_R > \tau_R$. Thus the variability

can be suppressed even while the typical events with $t_R \approx \tau_R$ are relatively unaffected by saturation.

To further evaluate our analysis with respect to the observed statistical properties of rod single photon responses (Whitlock and Lamb, 1999; Field and Rieke, 2002), we consider a time-resolved measure of response variability. Fig. 7 compares the time courses of the average response with the trial-to-trial standard deviation of the response all computed numerically in ensembles of simulated responses to receptor activation events with $P_n(t_R)$ distribution of shutoff times and $\tau_R k_H = 1.5$. The results show that the peak of $Q(t)$ lags behind the peak of the mean response, consistent with the results of Field and Rieke (2002).

We conclude, although we cannot prove here, that the spot-formation mechanism contributes to the high fidelity of single photon responses in rod cells. We have demonstrated that: 1), suppression of response variability is a natural consequence of the G-protein-mediated signaling cascade and 2), the proposed mechanism is not inconsistent with experimental observations of single photon response variability. Finally, we note that reduction of the coefficient of variation down to 0.25 is likely to be a multifactorial phenomenon with the abovementioned mechanism being one of several components.

APPENDIX: LOCALIZATION OF G-PROTEIN SIGNALING

In this Appendix we present the details of the calculations of the E^* spot formation by analyzing Eqs. 1 and 2. $[G^*]$ and $[E^*]$ are, respectively, the areal density of activated G-proteins and of activated effector, whereas $[E] = [E_{tot}] - [E^*]$ is the areal density of inactive or free effector. We are interested in the effect of a single activated receptor molecule, which we assume to be at the origin of our coordinate system, $r = 0$, and to stay active

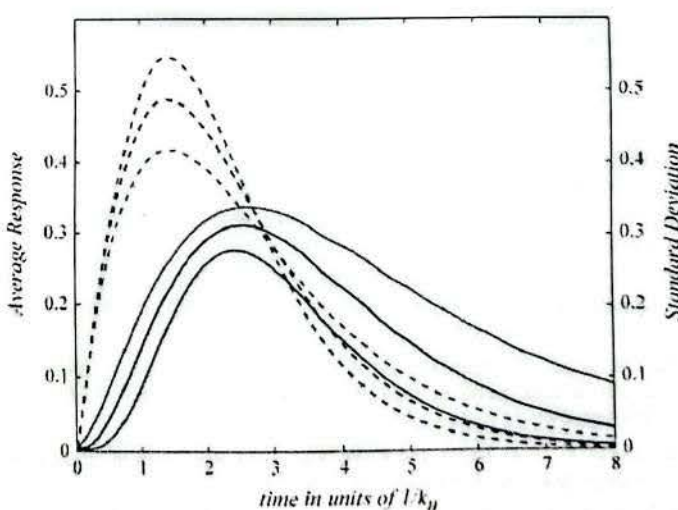


FIGURE 7 The time course of the trial-to-trial standard deviation (solid line) of the responses is compared to the time course of the average response (dashed line). Based on the same numerical simulation as Fig. 6 with $\tau_R k_H = 1.5$. Red, blue, and green curves correspond respectively to $n = 1, 2, 4$ shutoff steps. Note that the peak of standard deviation is delayed relative to the peak of the average response.

for time t , $0 < t < t_R$. Then active receptor areal density $[R^*] = \delta^{(2)}(r)\theta(t_R - t)\theta(t)$ where $\delta^{(2)}(r)$ denotes a two-dimensional Dirac delta function and function $\theta(t) = 1$ for $t \geq 0$ and equal to 0 for $t < 0$. In our further analysis, for the sake of simplicity we neglect the diffusion of E , since it does not qualitatively change the results. To produce full time-dependent solutions, equations were integrated numerically in MatLab (The MathWorks, Natick, MA).

Axially symmetric solutions are conveniently described in polar coordinates. To deal with the diffusion term, the solution was sought as a linear superposition of Bessel functions $J_0(\beta_m r)$ (Abramowitz and Stegun, 1965) where β_m forms the root of $J_0(z)$:

$$G^*(r, t) = \sum_m a_m(t) J_0(\beta_m r), E(r, t) = \sum_m b_m(t) J_0(\beta_m r).$$

Since Bessel functions are the eigen-functions of the Laplacian $\nabla^2 J_0(\beta r) = -\beta^2 J_0(\beta r)$, the partial differential equations (Eqs. 1 and 2) in the Bessel basis (i.e., in terms of a_m and b_m) reduce to a system of ordinary differential equations which are integrated numerically using an Adams-Basforth (Stoer and Bulirsch, 1992) method with the linear terms of Eq. 1 advanced in time using an implicit scheme (Stoer and Bulirsch, 1992). The nonlinear (k_2 term) is evaluated at the preceding time step by going back to r -space, i.e., by recomputing $G^*(r, t)$ and $E(r, t)$. Keeping 200 Bessel modes will provide sufficient convergence and allow rapid integration in MatLab.

Let us consider the stationary state, which can be reached in the absence of receptor deactivation:

$$\begin{aligned} k_1 \delta^{(2)}(r) - k_2 [E][G^*] + D_G \nabla^2 [G^*] &= 0, \\ k_2 [E][G^*] - k_H [E^*] + D_E \nabla^2 [E^*] &= 0. \end{aligned}$$

Eliminating the $k_2 [E][G^*]$ term and integrating the resulting equation over space removes the diffusion terms and yields an exact expression for the maximal number of activated E^* molecules in a saturated spot: k_1/k_H .

Authors acknowledge stimulating discussions with F. Rieke.

This work was supported in part by National Institute of General Medical Sciences grant No. GM67794 (to B.I.S.) and National Eye Institute grant No. EY02048 (to P.B.D.).

REFERENCES

- Abramowitz, M., and I. Stegun. 1965. Handbook of Mathematical Functions. Dover Publications, Mineola, NY.
- Albert, P. R., and L. Robillard. 2002. G-protein specificity: traffic direction required. *Cell Signal.* 14:407–418.
- Arshavsky, V. Y., T. D. Lamb, and E. N. Pugh, Jr. 2002. G-proteins and phototransduction. *Annu. Rev. Physiol.* 64:153–187.
- Baylor, D. A. 1996. How photons start vision. *Proc. Natl. Acad. Sci. USA.* 93:560–565.
- Baylor, D. A., B. J. Nunn, and J. L. Schnapf. 1984. Photocurrent, noise, and spectral sensitivity of rods of the monkey *Macaca fascicularis*. *J. Physiol.* 357:575–607.
- Baylor, D. A., G. Matthews, and K.-W. Yau. 1980. Two components of electrical dark noise in toad retinal rod outer segments. *J. Physiol.* 309:591–621.
- Baylor, D. A., T. D. Lamb, and K.-W. Yau. 1979. Responses of retinal rods to single photons. *J. Physiol.* 288:613–634.
- Berman, D. A., and A. G. Gilman. 1998. Mammalian RGS proteins: barbarians at the gate. *J. Biol. Chem.* 273:1269–1272.
- Birnbaumer, L. 1990. G-proteins in signal transduction. *Annu. Rev. Pharmacol. Toxicol.* 30:675–705.
- Brady, A. E., and L. E. Limbird. 2002. G-protein-coupled receptor interacting proteins: emerging roles in localization and signal transduction. *Cell Signal.* 14:297–309.
- Chabre, M., and P. Deterre. 1989. Molecular mechanism of visual transduction. *Eur. J. Biochem.* 179:255–266.
- Chen, C.-K., M. E. Burns, W. He, T. G. Wensel, D. A. Baylor, and M. I. Simon. 2000. Slowed recovery of rod photoreceptors in mice lacking the GTPase accelerating protein RGS9-1. *Nature.* 403:557–560.
- Colledge, M., and J. D. Scott. 1999. AKAPs: from structure to function. *Trends Cell Biol.* 9:216–221.
- Dumke, C. L., V. Y. Arshavsky, P. D. Calvert, M. D. Bownds, and E. N. Pugh, Jr. 1994. Rod outer segment structure influences the apparent kinetic parameters of cyclic GMP phosphodiesterase. *J. Gen. Physiol.* 103:1071–1098.
- Fagan, K. A., K. E. Smith, and D. M. F. Cooper. 2000. Regulation of the Ca^{2+} -inhibitable adenylyl cyclase type VI by capacitative Ca^{2+} entry requires localization in cholesterol-rich domains. *J. Biol. Chem.* 275:26530–26537.
- Field, G. D., and F. Rieke. 2002. Mechanisms regulating variability of the single photon response of mammalian rod photoreceptors. *Neuron.* 35:733–747.
- Gilman, A. G. 1987. G-proteins: transducers of receptor-generated signals. *Annu. Rev. Biochem.* 56:615–649.
- Gundermann, T., F. Kalkbrenner, and G. Schultz. 1996. Diversity and selectivity of receptor-G-protein interaction. *Annu. Rev. Pharmacol. Toxicol.* 36:429–459.
- Hamm, H. E., and M. D. Bownds. 1986. Protein complement of rod outer segments of frog retina. *Biochemistry.* 25:4512–4523.
- Hamer, R. D., S. C. Nicholas, D. Tranchina, P. A. Lieberman, and T. D. Lamb. 2003. Multiple steps of phosphorylation of activated rhodopsin can account for the reproducibility of vertebrate rod single-photon responses. *J. Gen. Physiol.* 122:419–444.
- He, W., C. W. Cowan, and T. G. Wensel. 1998. RGS9, a GTPase accelerator for phototransduction. *Neuron.* 20:95–102.
- Heck, M., and K. P. Hofmann. 1993. G-protein-effector coupling: a real-time light-scattering assay for transducin-phosphodiesterase interaction. *Biochemistry.* 32:8220–8227.
- Heck, M., and K. P. Hofmann. 2001. Maximum rate and nucleotide dependence of rhodopsin-catalyzed transducin activation: initial rate analysis based on a double displacement mechanism. *J. Biol. Chem.* 276:10000–10009.
- Helmreich, E. J. M., and K. P. Hofmann. 1995. Structure and function of proteins in G-protein-coupled signal transfer. *Biochim. Biophys. Acta.* 1286:285–322.
- Kahlert, M., and K. P. Hofmann. 1991. Reaction rate and collision efficiency of the rhodopsin-transducin system in intact retinal rods. *Biophys. J.* 59:375–386.
- Lamb, T. D. 1994. Stochastic simulation of activation in the G-protein cascade of vision. *Biophys. J.* 67:1439–1454.
- Leskov, I. B., V. A. Klenchin, J. W. Handy, G. G. Whitlock, V. I. Govardovskii, M. D. Bownds, T. D. Lamb, E. N. Pugh, Jr., and V. Y. Arshavsky. 2000. The gain of rod phototransduction: reconciliation of biochemical and electrophysiological measurements. *Neuron.* 27:525–537.
- Lodish, H., A. Berk, S. L. Zipursky, P. Matsudaira, D. Baltimore, and J. Darnell. 2000. Molecular Cell Biology, 4th Ed. W.H. Freeman, New York. 849–877.
- Makino, C. L., J. W. Handy, T. Li, and V. Y. Arshavsky. 1999. The GTPase activating factor for transducin in rod photoreceptors in the complex between RGS9 and type 5 G-protein β -subunit. *Proc. Natl. Acad. Sci. USA.* 96:1947–1952.
- Okamoto, T., A. Schiegel, P. E. Scherer, and M. P. Lisanti. 1998. Caveolins, a family of scaffolding proteins for organizing “preassembled signaling complexes” at the plasma membrane. *J. Biol. Chem.* 273:5419–5422.
- Pugh, E. N., Jr., and T. D. Lamb. 1993. Amplification and kinetics of the activation steps in phototransduction. *Biochim. Biophys. Acta.* 1141:111–149.

THE JOURNAL OF PHYSICAL CHEMISTRY B

Subscriber access provided by University of South Dakota

B: Biophysics; Physical Chemistry of Biological Systems and Biomolecules

Effect of the Organization of Rhodopsin on the Association Between Transducin and a Photoactivated Receptor

Samuel Andres Ramirez, and Chad Leidy

J. Phys. Chem. B, Just Accepted Manuscript • DOI: 10.1021/acs.jpcb.8b07401 • Publication Date (Web): 29 Aug 2018

Downloaded from <http://pubs.acs.org> on August 30, 2018

Just Accepted

"Just Accepted" manuscripts have been peer-reviewed and accepted for publication. They are posted online prior to technical editing, formatting for publication and author proofing. The American Chemical Society provides "Just Accepted" as a service to the research community to expedite the dissemination of scientific material as soon as possible after acceptance. "Just Accepted" manuscripts appear in full in PDF format accompanied by an HTML abstract. "Just Accepted" manuscripts have been fully peer reviewed, but should not be considered the official version of record. They are citable by the Digital Object Identifier (DOI®). "Just Accepted" is an optional service offered to authors. Therefore, the "Just Accepted" Web site may not include all articles that will be published in the journal. After a manuscript is technically edited and formatted, it will be removed from the "Just Accepted" Web site and published as an ASAP article. Note that technical editing may introduce minor changes to the manuscript text and/or graphics which could affect content, and all legal disclaimers and ethical guidelines that apply to the journal pertain. ACS cannot be held responsible for errors or consequences arising from the use of information contained in these "Just Accepted" manuscripts.

→ ¿cuáles son las estructuras?
↳ estáticas cristales
↳ dinámicas monómeros

Transducina se unen dentro de cristales
fundamentales de rodopsina.



ACS Publications

is published by the American Chemical Society, 1155 Sixteenth Street N.W.,
Washington DC 20036
Published by American Chemical Society. Copyright © American Chemical Society.
However, no copyright claim is made to original U.S. Government works, or works
produced by employees of any Commonwealth realm Crown government in the course
of their duties.

4
5
6
7
8
9
10
11
12
13
14
15
16
17
18
19
20
21
22
23
24
25
26
27
28
29
30
31
32
33
34
35
36
37
38
39
40
41
42
43
44
45
46
47
48
49
50
51
52
53
54
55
56
57
58
59
60

ABSTRACT: After photoactivation, rhodopsin (R), a G-protein-coupled receptor, rapidly activates multiple transducin G-proteins (G) in an initial amplification step of phototransduction. G-protein activation requires diffusion mediated association with an active rhodopsin (R^*) at the rod disc membrane. Several microscopy studies have revealed different organizations of R within the membrane, including static and freely diffusing situations. However, it is unclear how such different scenarios influence the activation rate of G proteins. Through Monte Carlo simulations, we study the association reaction between a photoactivated rhodopsin (R^*) and transducin under different reported receptor organizations including: a) R monomers diffusing freely, b) R forming static, dispersed crystalline domains made of rows of dimers, and c) R arranged in static tracks formed by two adjacent rows of dimers. We perform simulations varying the probability of binding following a collision (p). For high p , the association rate between R^* and G is higher in the freely diffusive system than in the static organizations, but for low collision efficiencies, the static organizations can result in faster association rates than the mobile system. We also observe that with low p , increasing the concentration of R increases the association rate significantly in the dispersed crystals configuration and just slightly in the free diffusive system. In summary, the lateral organization of rhodopsin influences the association rate between R^* and G in a manner strongly dependent on the collision efficiency.

$$V = \frac{P}{t} \quad \times V t = P \quad \therefore I = \frac{V P}{\tau}$$

INTRODUCTION

At night, our visual system can resolve signals as weak as a few photons per second. Two of the requirements to achieve this outstanding sensitivity are a high efficiency of photon capture at rod photoreceptor cells, and subsequent amplification of this event into a significant electrical signal in the rod cell ¹. Photons are absorbed by rhodopsin (R), a G-protein-coupled receptor found at high concentration at the membrane of the discs in the rod outer segment. The elevated number of rhodopsin molecules in the discs accounts for an efficient photon capture. Upon absorption of a photon, R becomes activated and triggers a cascade of reactions that results in photoresponse amplification. The first step in this cascade, crucial for signal amplification, is the rapid activation of many G-protein transducins (G) by a photoactivated rhodopsin (R*). Transducin activation requires the lateral encounter and binding between G and R*, and the subsequent exchange of GDP for GTP in the alpha subunit of transducin mediated by R*.

Fusion somellos

Early research on phototransduction proposed that rhodopsin molecules within the disc membrane existed as monomers that underwent rapid lateral diffusion ^{2,3}. Such observations prompted researchers to hypothesize that the fast lateral diffusion of rhodopsin was essential for the rapid encounters between R* and G required for fast G activation. However, more recent experiments using atomic force microscopy, electron microscopy, and biochemical approaches ⁴ have revealed that rhodopsin can be found on the disc membrane as static dimers forming oligomeric structures also called nanodomains. Furthermore, a reappraisal of the lateral diffusion of rhodopsin indicates that there is a fraction of immobile receptors that can vary between zero and 100%, and it is likely that the immobile fraction corresponds to receptors forming nanodomains ^{11,12}. These observations have motivated a re-evaluation of the effect of R mobility and organization on the initial steps of phototransduction ^{12,13}.

Computational studies have concluded that a static configuration of R is still compatible with the rapid activation of G proteins, as the fast diffusion of transducin can account for a high frequency of lateral encounters with an immobile R ^{10,14,15}. Such studies have also suggested that scenarios with static R result in a slower rate of G activation compared with situations where R*

nanodomains regiones celulares que forman un espacio
ACS Paragon Plus Environment

para la señalización que regulan los procesos

can diffuse. Using Monte Carlo simulations on a discrete grid, Dell'Orco and Schmidt¹⁴ looked at the first encounter time between a single R* and transducin molecules. They observed that for a high concentration of R, an organized static configuration of dimeric receptors results in faster first-encounters compared to a scenario with unorganized static rhodopsin. Nevertheless, allowing R to freely diffuse, while maintaining the diffusivity of G at its physiological value will result in faster first encounter times compared to the static organized configuration due to higher overall mobility in the freely diffusive scenario. Schoneberg et al. 2014 used a Brownian dynamics approach to model the different steps that lead to the activation of transducin upon activation of a single R¹⁵. Their simulations suggested that an organization where inactive dimeric rhodopsins form static compact racks while the activated receptor can diffuse freely, results in a similar rate of G activation as the case where all receptors diffuse in monomeric form. However, if R* forms part of a rack, the activation rate of G is significantly reduced compared to the freely diffusing scenario. In a subsequent study, Gunkel et al. 2015 described experimentally and simulated a configuration where R is organized in tracks made of two adjacent rows of dimers¹⁶. They also observed that a freely diffusive scenario yields a faster encounter rate than the tracks configuration. Overall, these studies observed faster R*-G first encounters in a free diffusive system compared to a static R* situation, and this can result in faster G activation in the mobile system. However, in a setting where the probability of association between R* and G following an encounter is low, in addition to the frequency of first encounters, re-encounters may also influence the rate of G activation^{16,17}.

Here we perform Monte Carlo simulations of the diffusion mediated association between R* and G at the disc membrane. In our simulations transducin binds R* with probability p upon collision. Furthermore, a binding event can occur only when G collides with R* at certain positions (active sites), which reflects better the physiological situation. We consider three organizations of rhodopsin in the membrane: a) the classic view where rhodopsin molecules diffuse as monomers, b) a system where rhodopsin is found as static dispersed crystals made of rows of dimers and c) an organization where rhodopsin is arranged in static tracks made of 2 adjacent rows of dimers. We observe that, compared to the freely diffusive configuration, the static organizations of receptors can result in higher, lower or similar association rates between R* and G, with the outcome depending on the collision efficiency p .

METHODS

Monte Carlo simulations were carried out in a triangular grid (rhombus shaped domain) with periodic boundary conditions and lattice size $\Delta x = 1.2\text{nm}$. In this setting pixels are rhombi with area $3^{1/2}\Delta x^2/2$. R monomers and G proteins were represented by hexagonal arrays of 7 and 19 pixels respectively (Fig 1 b) resulting in an effective protein size of 3nm for R and 5nm for G, which are values close to physiological estimates ^{18,19}. Rhodopsin is a transmembrane protein and transducin is a peripheral protein anchored to the membrane by means of lipid modifications in its alpha and gamma subunit. This allows G to protrude farther away from the membrane leading to an umbrella-like overlap between R and G when these two proteins approach each other ²⁰. To account for this difference in the positioning at the membrane in our simulations, G proteins can partially overlap with rhodopsin proteins as shown in Fig. 1 b. For simplicity, we represented just one lipid modification of transducin as a pixel at the center of the protein, and this anchor cannot overlap with R following Dell'Orco and Schmidt 2008 ¹⁴. We tracked the number of binding events between an R* and different transducin molecules. Once a particular G has reacted, it keeps diffusing but cannot bind the same photoactivated receptor again. To avoid artificial effects due to depletion of G as they react, we selected the size of the grid so that no more than 7% of the pool of transducins react with an R* during a simulation. Following this criterion, the side L of the grid was $\sim 1\mu\text{m}$.

Rhodopsin supramolecular configuration. As described in the introduction, rhodopsin can form higher order structures made of rows of stacked dimers in the disc membrane. We represent a dimer with two adjacent hexagonal rhodopsins resulting in a separation between monomer centers of $\sim 3.2\text{nm}$ (Fig. 1 d). Dimers are set in three possible orientations that follow from rotations without considering mirror reflections (Figs. 1 c, 1 d). Rows were made of stacked dimers such that G proteins can diffuse across rows ^{10,14}.

Separate studies have reported different configurations of the rows of dimers. Here we simulate the following representative organizations: a nanodomains scenario with dispersed crystals each one made of rows aligned next to each other, a configuration with dispersed tracks

No entiendo bien que son esos cristales 11

each one formed by 2 adjacent rows of dimers¹⁰, the classic scenario where monomers of rhodopsin freely diffuse, and a configuration with immobile rhodopsin monomers randomly located in the membrane. To generate the dispersed crystals configuration, we first allocate a number of dimers at random locations and with random orientations. These dimers act as nucleation seeds for the crystals! To grow the crystals, a seed is selected arbitrarily and one dimer is added in a randomly selected position along the perimeter of the growing crystal. The growth process continues until a specified fraction of area covered by rhodopsin (f) is reached. We used a density of 593 seeds/ μm^2 , so that at full coverage of receptors, we obtain an arrangement qualitatively similar to the compact arrangement reported by Fotiadis et al. in 2003⁸. The tracks configuration is generated with an analogous crystal-growing procedure as before, but seeds are track units: 2 dimers, each one belonging to one of the rows forming the track. Such seeds are then randomly added in either the front or the back of the growing track. We adjusted the number of seeds in this case to obtain a particular average track length at the physiological concentration of R. Gunkel et al., 2015 reported a minimum length of 10 dimers in a row per track. We ran simulations with average lengths of 10, 15, and 20 dimers in a row per track. The kinetics were similar in each of these cases (Supporting Information).

Random walk simulations. For every time step, every mobile protein in the simulations is selected and allowed to move one step Δx with probability p_{jump} . The direction of the movement is selected randomly from the six possible directions on the grid. If there is an obstruction in the new position of the protein the jump is rejected. We determined the effective diffusion coefficient of a protein as:

$$D_{\text{eff}} = \frac{\langle r^2 \rangle}{4t_f}$$

where $\langle r^2 \rangle$ is the mean squared displacement for a time interval of $t_f = 60\text{ms}$. In the absence of obstructions, the effective diffusion coefficient is known to be $D_{\text{max}} \times p_{\text{jump}}$, where $D_{\text{max}} = \Delta x^2/(4\Delta t)$. We used a time step $\Delta t = 0.18\mu\text{s}$ so that $D_{\text{max}} = 2\mu\text{m}^2/\text{s}$. However, in the presence of obstacles (e.g. other proteins in the membrane), the effective diffusion coefficient will be less than $D_{\text{max}} \times p_{\text{jump}}$. We adjusted p_{jump} so that the effective diffusion coefficients in the monomeric diffusive configuration matched the experimentally determined values at physiological concentrations of R and G. In this case, the concentrations of R and G are $25000/\mu\text{m}^2$ and

$2500/\mu\text{m}^2$ respectively, and the effective diffusion coefficients are $D_R \sim 0.4\mu\text{m}^2/\text{s}$ for rhodopsin¹¹ and $D_G \sim 1.0\mu\text{m}^2/\text{s}$ for transducin²¹. The adjusted values of p_{jump} were 0.34 for R and 0.75 for G. These parameters were not modified in our simulations, except for the configurations where rhodopsin is static, in this case $p_{\text{jump}} = 0$ for R. The number of trajectories used to estimate D_{eff} varied between ~ 130000 and ~ 500000 for R and between ~ 20000 and ~ 30000 for G.

Simulation of reactions. Upon a collision, G and R* can bind with probability p (collision efficiency). Once a transducin has participated in a binding event it remains diffusing on the grid but can no longer react with the same R*. We count a collision when one protein, or both, attempt to jump into the grid points occupied by the other protein, and the center of G is located in one of the active sites around R* (Fig. 1 b, d). The reaction is tried with probability p if the center of G is still in an active site after both proteins attempted to move during a timestep of the simulation. This is to avoid reactions when one protein jumps towards the other, but the later jumps away from the former during the same Δt . We consider a limited number of active sites for R* to reflect the fact that G must approach a rhodopsin molecule from a particular direction in order to bind it²⁰. In the main text we present results using 5 active sites. Changing this parameter does not change our conclusions as shown in the Supporting Information.

Association rate constant k . We estimated k from the average rate of binding events N_{bind} after $t_f = 60\text{ms}$ as :

$$k = \frac{\langle N_{\text{bind}} \rangle}{t_f [G]}$$

where [G] is the concentration of G ($2500/\mu\text{m}^2$).

The first-encounter rate is calculated as $\langle N_{\text{bind}} \rangle/t_f$ from simulations where G binds R* immediately once they are in proximity.

To increment the data acquisition in a single simulation, multiple rhodopsins are randomly labeled as R*. The binding reactions are tracked independently for each R* without crosstalk between R*'s: a G protein that has bound a particular R* but has not reacted with a second one, can bind the second R*. For the monomeric diffusive and random static distributions, k was

estimated from a total number $N_{R^*} = 20000$ of activated receptors. For the dispersed crystals and tracks configurations $N_{R^*} = 10000$. The standard error of k was computed as:

$$SE(k) = \frac{SD(N_{bind})}{t_f[G]N_{R^*}^{1/2}}$$

where $SD(N_{bind})$ is the standard deviation of N_{bind} .

Diffusive and reactive rate constants (k_D and k_r). These rates were obtained from a fit to the data of $1/k$ vs. $1/p$ as shown in Fig. 2, b. The statistical error in the values of k_D and k_r was obtained from the standard deviation of three independent estimations.

Software and performance. The simulations were implemented in C++, the code is available upon request. The CPU time for a simulation of 60ms depended on the setting. When run on a computer with 32GB memory and 3.5 GHz Intel Core i7 processor, a typical simulation with a static rhodopsin configuration took ~210s CPU time, and for a free diffusing scenario this time varied between 670s and 2700s depending on the concentration of receptors.

RESULTS AND DISCUSSION

By means of Monte Carlo simulations we studied how the organization of rhodopsin in the membrane affects the association reaction between a single photoactivated rhodopsin and transducin molecules. First we considered a scenario where rhodopsin molecules are found as monomers that diffuse freely in the membrane (Fig. 1, *a* and *b*), and a configuration where the receptors form dispersed static crystals made of rows of dimers (Fig. 1, *c* and *d*). We simulated the lateral diffusion of G proteins (and rhodopsin molecules in the monomeric diffusive scheme) in a triangular grid (Fig. 1, *b* and *d*). In our simulations a binding event will occur with probability p upon collision between R^* and transducin (see Methods). We estimate the rate constant k of the association reaction between a single R^* and G as the rate of average binding events (Fig. 2 *a*) divided by the concentration of transducin.

la geometría es
muy importante?

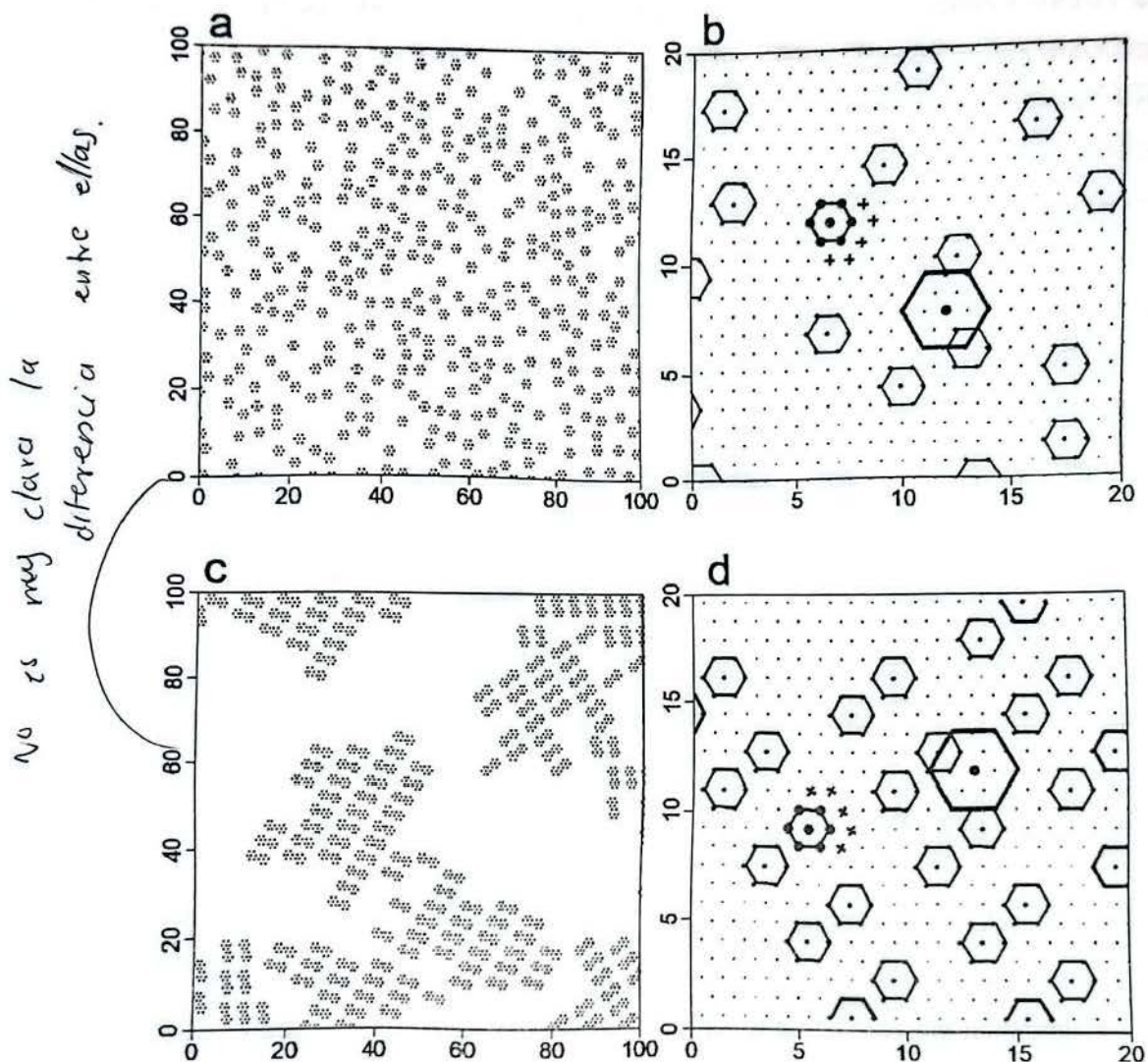


FIGURE 1 Representation of rhodopsin and transducin molecules on the triangular grid. (a) Monomeric diffusive scheme. (b) Magnification of a region of the area in *a* showing individual rhodopsin monomers. We also include a transducin shown as a blue hexagon and a photoactivated rhodopsin shown as a red hexagon. Red crosses indicate the active sites of the photoactivated rhodopsin. (c) Example of the arrangement of rhodopsin molecules in the dispersed crystals scheme. A crystal is made of adjacent rows of dimers with the same orientation. (d) Magnification of a region of the area in *c* showing individual dimers of R stacked in rows. A transducin, a photoactivated R and the active sites of R* are shown with the same format as in *b*. *a* and *c* are patches from grids containing the physiological concentration of R.

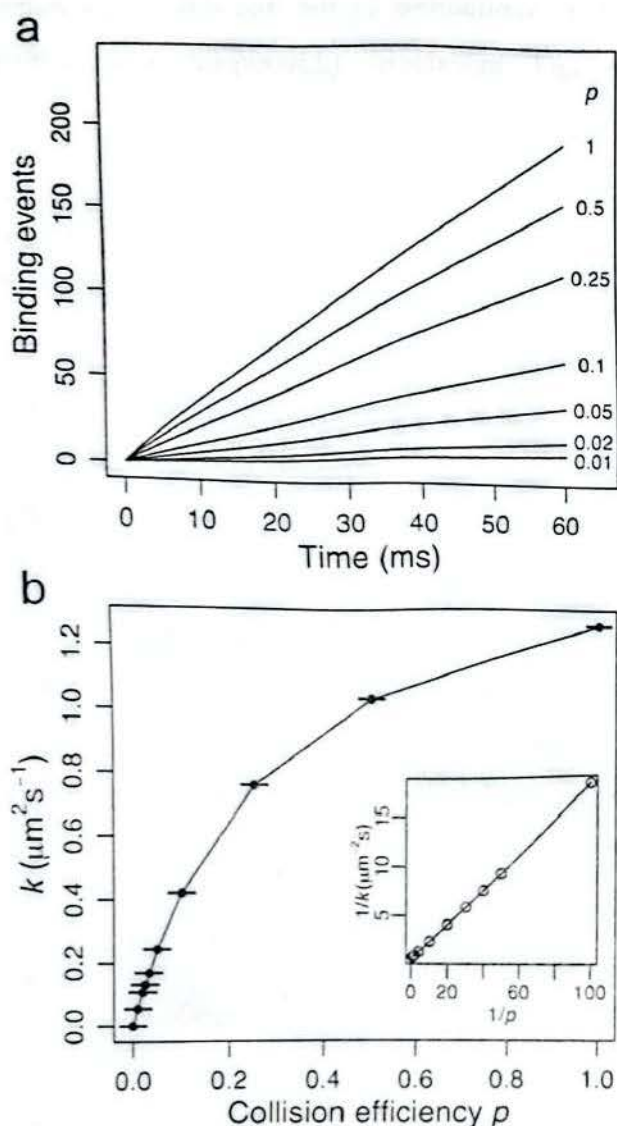
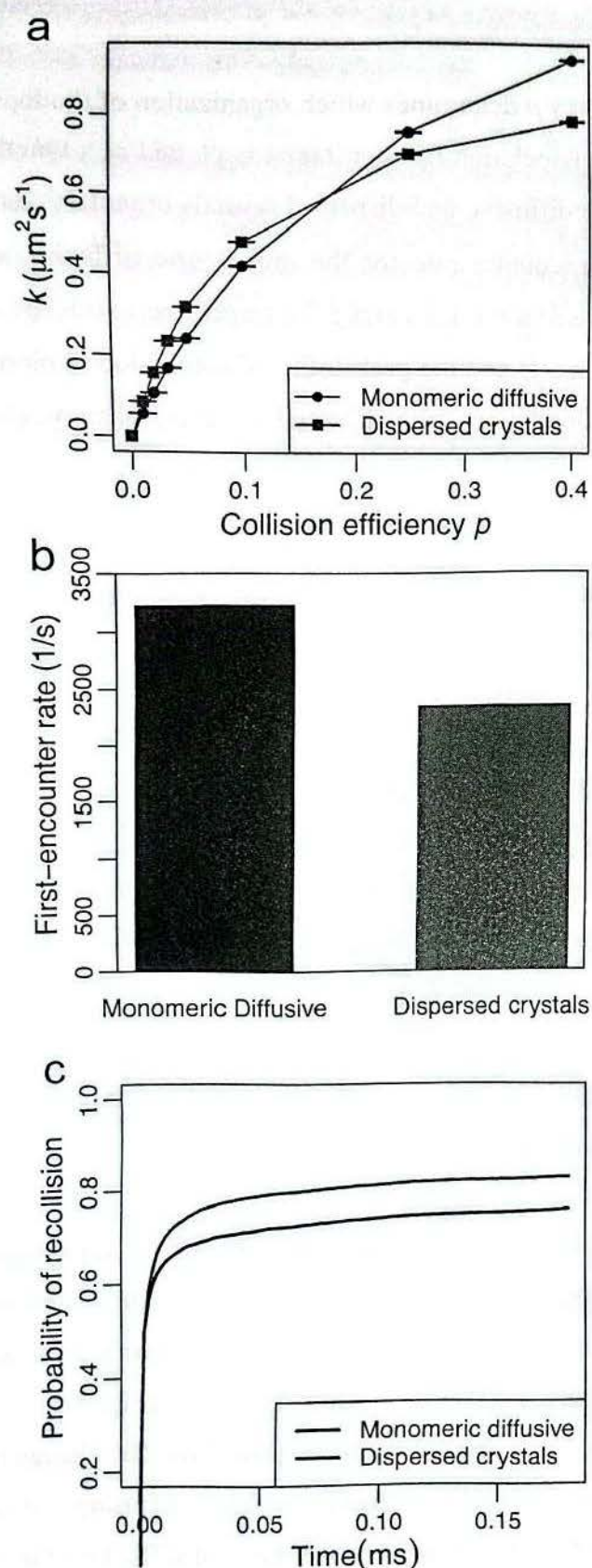


FIGURE 2 Estimation of the association rate constant k , the diffusive rate constant k_D and the reactive rate constant k_R . (a) The time series of average binding events between G and R* shows a linear trend for each value of the collision efficiency p simulated. This shows that the change in abundance of G during a simulation is not significant enough to affect k dramatically. (b) The association rate constant k is calculated as the average binding events at $t = 60$ ms divided by the concentration of G and t , and is plotted as a function of the collision efficiency p . Error bars are ± 2 SE. Inset: Eq. 1 was fit to the data in b to determine the first-encounter rate constant k_D and the reactive rate constant k_R . In this case, the rate constants were calculated to be $k_D = 1.63 \mu\text{m}^2\text{s}^{-1}$

¹ and $k_R = 5.72 \mu\text{m}^2/\text{s}$. The data corresponds to simulations of the free diffusing scenario at physiological concentration of rhodopsin and transducin ($25000/\mu\text{m}^2$ and $2500/\mu\text{m}^2$ respectively).

The association rate, k , is higher in the freely diffusive system than in the dispersed crystals configuration when the collision efficiency is high (Fig. 3 a). In this regime, a faster rate of first-encounters in the monomeric diffusive configuration compared to the dispersed crystals system (Fig. 3. B) results in a higher association rate in the former than in the later arrangement. The higher first-encounter rate in the freely diffusive system is expected due to a higher total diffusivity ($D = D_R + D_G = 1.4 \mu\text{m}^2/\text{s}$) as compared to the static configuration where only G diffuses ($D = 0.91 \mu\text{m}^2/\text{s}$). However, for low collision efficiencies, the association rate is faster in the dispersed crystals configuration compared to the monomeric diffusing scenario (Fig. 3 a). In this case, a binding event is not likely to occur upon an initial encounter between R* and G, however, a higher probability of recollision in the dispersed crystals configuration (Fig. 3 c) increases the chance of binding between two molecules that are in close proximity, therefore enhancing the association rate ^{16,22}.



monomero: molécula individual con potencial a unirse a otras.

cristales: sólido organizado que surgen del orden repetido de molecular.

FIGURE 3 The value of the collision efficiency p determines which organization of rhodopsin results in a faster association kinetics. (a) The association rate constant k is plotted as a function of the collision efficiency p for the monomeric diffusive and dispersed crystals organizations of rhodopsin. Error bars are ± 2 SE. (b) First-encounter rate for the monomeric diffusive and dispersed crystals configurations, the standard errors are 1.5/s and 5.7/s respectively. (c) The re-encounter time is tracked for 10000 collision events and the probability of recollision is plotted as a function of time for both scenarios. The simulations are performed using the physiological concentration of R.

The contribution of the first-encounters and recollisions to the association rate can be expressed quantitatively as:

$$\frac{1}{k} = \frac{1}{k_D} + \frac{1}{p \times k_R} \quad (1)$$

where k_D is a diffusive rate constant related to the first-encounter rate between reactants and k_R is a reactive constant related to the probability of recollision upon an unreactive collision¹⁷. Equation (1) shows in mathematical form how the collision efficiency p modulates the contribution of k_D and k_R to the association rate. Furthermore, these constants can be determined by fitting Eq. 1 to our association rates data (for example see Fig. 2 b and inset). To better understand how the organization of rhodopsin influences the association rate constant k by separately influencing first-encounters and recollisions, we show below how k_D and k_R behave for different configurations and concentrations of the receptors.

For all R concentrations tested, the diffusive rate constant k_D is higher in the monomeric diffusive system compared to the dispersed crystals configuration (Fig. 4 a). This is in agreement with a higher first-encounter rate (Fig. 3 b) due to the higher mobility in the freely diffusive system. For higher concentrations of R, D decreases due to obstruction effects (Fig. 4 c) and consequently the reactive constant k_D is reduced in both configurations (Fig. 4 a). The change in k_D , however, is more gradual in the dispersed crystals scheme than in the freely diffusing system (Fig. 4 a). This observation is in part explained by a similar trend for the total diffusion (Fig. 4

c), where D decreases slower in the dispersed crystals configuration than in the monomeric diffusive system with higher levels of R.

To investigate how the particular organization of R in the dispersed crystals scenario influences k_D , we also ran simulations for a static non-crystallized configuration where R monomers are randomly allocated and remain immobile (Fig. 4 a, open circles). This configuration results in a diffusion coefficient ($D = D_G$) comparable to the dispersed crystals organization at moderate concentrations of R (Fig. 4 c). Interestingly, k_D is lower in the dispersed crystals configuration compared to the static random scheme at low concentrations of R, despite having a similar or higher D (compare Fig. 4 a and c). The reduced k_D in the dispersed crystals configuration is likely related to the clustering of rhodopsin molecules into oligomeric structures, which hampers the arrival of new G proteins to the photoactivated receptor. In contrast, the static random configuration is characterized by R proteins with no neighbors, and this arrangement facilitates first encounters between R^* and G for low levels of R. As we increase the concentration of R, however, k_D is no longer higher in the static random arrangement compared to the dispersed crystals configuration; in agreement with¹⁴, the organized static configuration results in higher diffusive rate constant than the unorganized scheme. This is a consequence of a greater reduction in protein mobility in the random static scenario than in the dispersed crystals configuration as the levels of R increase (Fig. 4 c). We note that even at the highest density of R shown here, the static random configuration is at a concentration below the percolation threshold²³, therefore, the reduction in k_D is attributed mainly to a reduction in the normal diffusion due to obstacles and not due to trapping of G proteins in finite regions bounded by receptors.

partículas
se unen
y se forman
agrupaciones

partículas
se enlazan
y se convierten
en conductores

aparece por

primera vez una

conexión continua

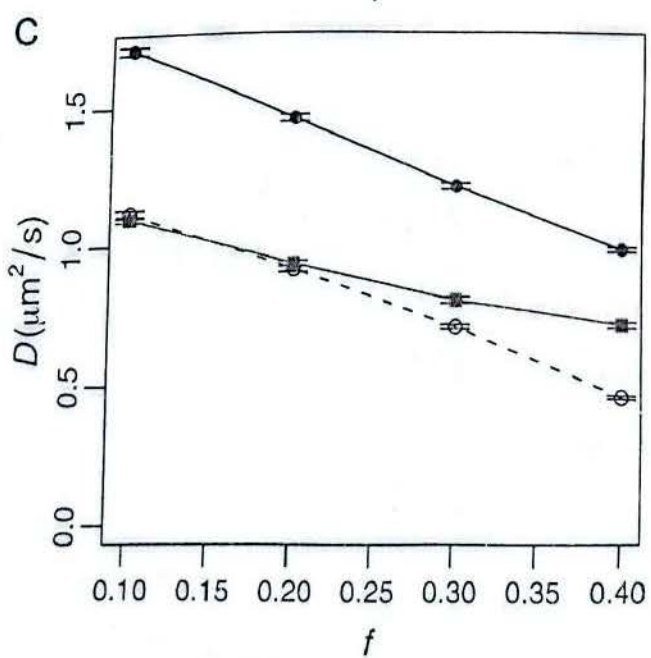
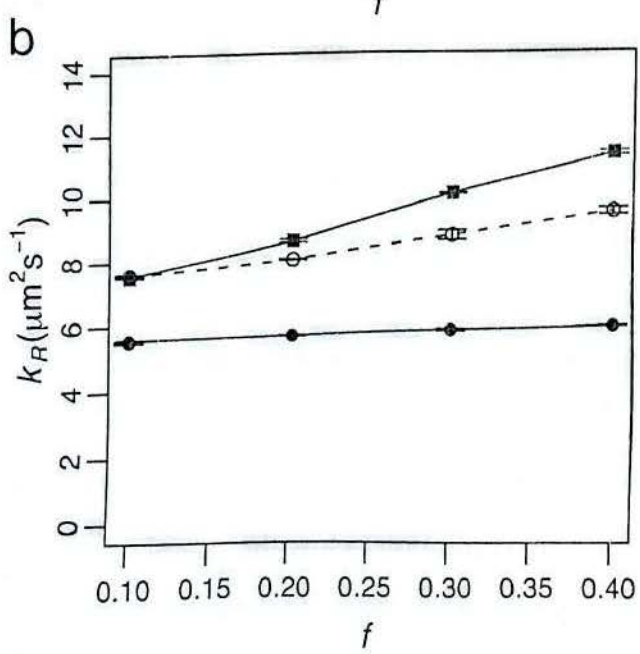
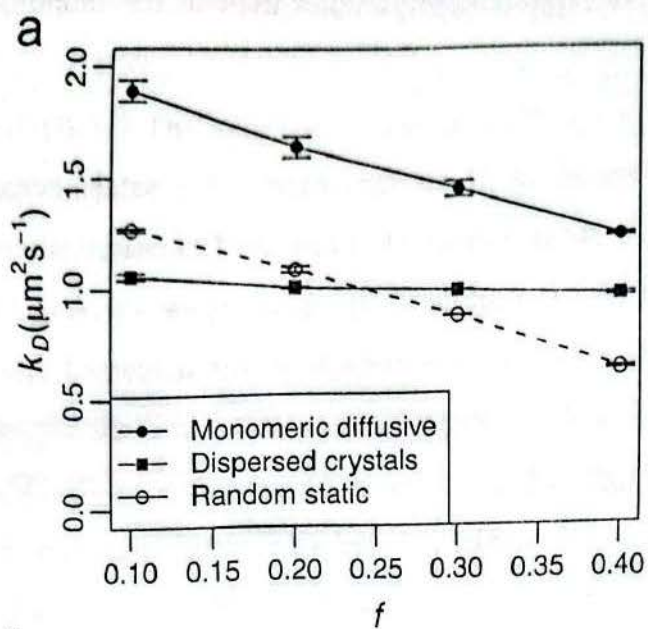


FIGURE 4 Effect of the concentration of R (expressed as the fraction of covered area f) on the diffusive rate constant k_D (a), the reactive rate constant k_R (b), and the total diffusion coefficient D (c) for the monomeric diffusive (*solid black circles*) and dispersed crystals (*red squares*) scenarios. In *open circles* we show results for a configuration where rhodopsin monomers are static and randomly allocated. In (a) and (b) the error bars are ± 2 standard deviations from 3 independent estimations of k_D and k_R . In (c) the error bars are ± 2 standard errors.

Debido a que las moléculas estarán más cercanas en la reg. 3a.

In contrast to k_D , the reactive constant k_R is higher in the dispersed crystals configuration compared to the monomeric diffusing scheme (Fig. 4 b). This is in agreement with a higher probability of recollision in the former configuration (Fig. 3 c). Furthermore, while in the monomeric diffusive system k_R has a weak dependence on the concentration of receptors, in the dispersed crystals organization k_R increases significantly as the levels of R increase (Fig. 4 b). To identify effects from the particular organization of the receptors in the dispersed crystals configuration, we compute k_R for the static random configuration of R as well (Fig. 4 b, *open circles*). The dispersed crystals configuration shows a higher k_R than the static random scheme, indicating that the organized arrangement of interspersed R dimers results in a higher probability of recollisions between R^* and G.

As discussed before, the association rate depends on both the first-encounter rate and the probability of recollisions, and such dependence can be expressed by Eq. (1) via k_D and k_R where it is evident that the collision efficiency p modulates the contribution of those factors. When p is high, for example, the first-encounter rate is dominant and the association rate constant k behaves as k_D (compare Figs. 4 a and 5 a). In this case the monomeric diffusive system results in higher k than the dispersed crystals configuration, and the association rate constant decreases with higher concentration of R in both cases (Figs. 4 a and 5 a). In contrast, for low collision efficiency, recollisions are more important, and k shows a similar behavior as k_R . In this regime, the dispersed crystals configuration results in higher association rates than the monomeric diffusive system. Furthermore, k increases with higher levels of R in the dispersed crystals configuration, but remains mostly unchanged in the monomeric diffusive system. (Figs. 4 b and 5 b).

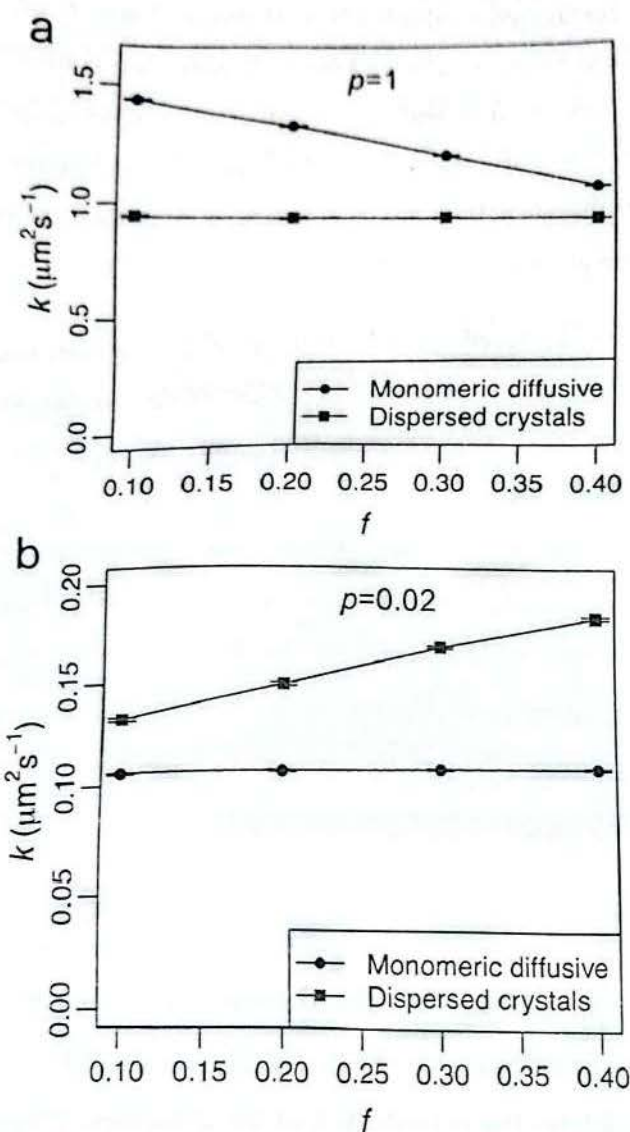


FIGURE 5 The trend of the association rate constant k as a function of the concentration of R depends on the collision efficiency. (a) High collision efficiency ($p = 1$). (b) Low collision efficiency ($p = 0.02$). Error bars are ± 2 SE.

Lastly, we considered a configuration where rhodopsin is organized in tracks of two adjacent rows of dimers, based on recent observations by Gunkel et al.¹⁰ (Fig. 6A). Surprisingly, this organization yields very similar binding rates compared to the dispersed crystals configuration, showing faster association than the monomeric diffusive scenario for low collision efficiencies, and slower rates than the mobile system for larger values of p . These results suggest that the enhanced recollisions that foster binding rates at low p are mostly attributed to static receptor

dimers interspaced with free membrane where G can diffuse across, and whether the higher order structures are tracks or dispersed crystals does not have a major impact.

Gunkel et al. 2015¹⁰ proposed that the tracks organization in combination with transient association of G with inactive R^{24,25} can result in trapping of G proteins in the tracks, a phenomenon that they called kinetic trapping. Upon photoactivation of a single rhodopsin, the G proteins trapped in the track containing R* will be activated more rapidly than G proteins coming from other tracks resulting in a biphasic response¹⁰. We argue that kinetic trapping should be facilitated by recollisions, as repeated encounters between G and R will enhance the formation of non-productive R-G complexes. Furthermore, in such a scenario, G proteins could be enriched in nanodomains and depleted in membrane regions free of rhodopsin, as recollision-enhanced association with R could promote longer residence times of G in areas with high density of R. As our results indicate that recollisions are similar in crystals and tracks configurations, we suggest that kinetic trapping and perhaps G enrichment in nanodomains may be possible in both types of architectures.

→ No entiendo bien en qué
consisten las trampas esa.

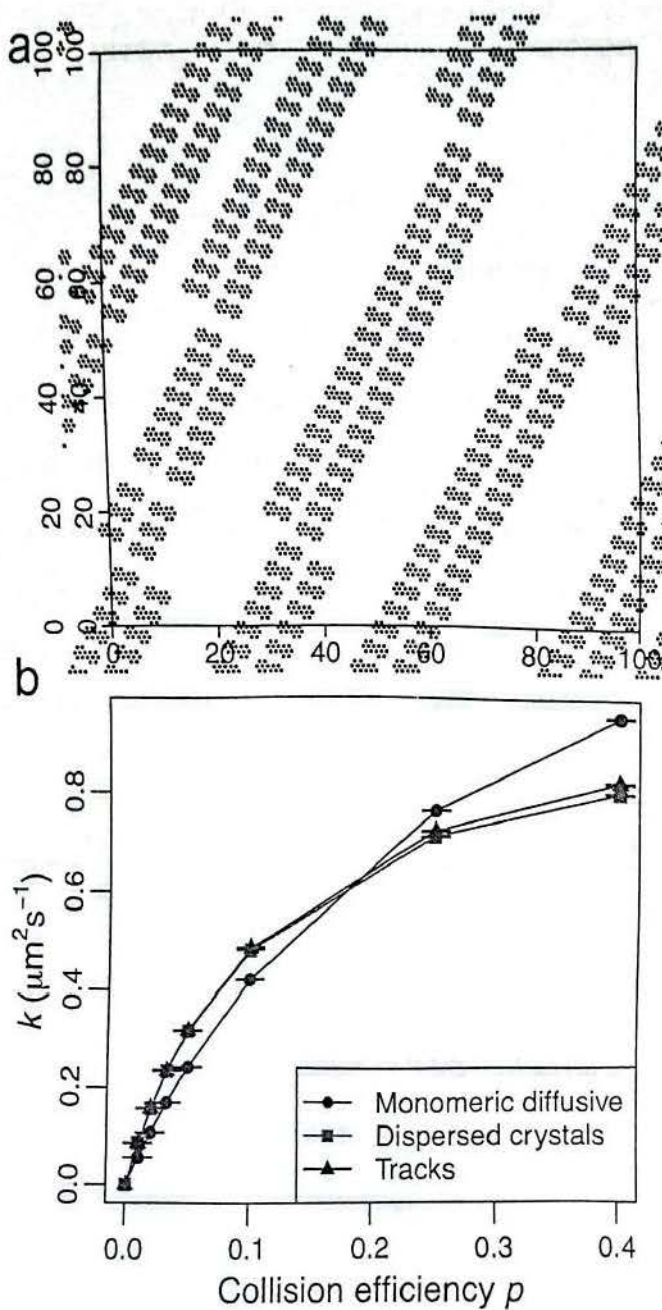


FIGURE 6 An organization where the receptors are arranged in tracks results in similar association rates than the dispersed crystals configuration. (a) In the tracks organization, adjacent rows of dimers form “canals” free of receptors. (b) Association rate constant k for the monomeric diffusive, dispersed crystals and tracks organizations as a function of the collision efficiency p . Error bars are ± 2 SE.

Overall, our results suggest that the effect of the configuration of rhodopsin on the association rate between R^* and G depends dramatically on the probability of binding upon collision. The

collision efficiency of this reaction is believed to be low²⁶, therefore, the aggregation of receptors into static ordered configurations may result in a kinetic advantage over a configuration where monomeric R freely diffuses. As we present here, such a kinetic advantage is due to enhanced recollisions between R* and G.

In this work, we considered how the organization of rhodopsin can influence the association reaction between R* and G due to volume exclusion effects. These effects may have further consequences on photon detection²⁷ by affecting other reactions occurring at the disc membrane, for example, the phosphorylation of R* by rhodopsin kinase, the activation of cGMP phosphodiesterase by activated transducin and deactivation of transducin mediated by RGS proteins²⁸. Investigating how the organization of rhodopsin can affect such reactions is a possible extension of this study. Furthermore, the effects that we study here may be applicable to other GPCR systems where the receptors aggregate forming oligomers in the membrane²⁹⁻³².

CONCLUSIONS

20 - 30
unidades.

By means of Monte Carlo simulations, we studied how different organizations of rhodopsin in the membrane influence the association reaction between a photoactivated receptor and transducin. We considered three plausible scenarios: (a) rhodopsin molecules diffuse on the membrane in monomeric form, (b) the receptors are arranged in static dispersed crystals made of rows of dimers, and (c) rhodopsin molecules are assembled in static tracks made of two adjacent rows of dimers.

The collision efficiency p determines how the configuration of rhodopsin affects the association rate between G and R*. For high p , the association rate is higher in the scenario where rhodopsin molecules diffuse as monomers. However, for low collision efficiencies, k is higher in the structured static configurations. The tracks arrangement and the dispersed crystals configuration result in similar association rates.

Higher concentrations of R will promote recollisions between G and the receptor and can enhance association for low collision efficiencies. This tendency is stronger for configurations

with organized static receptors and is weak for a scenario where R monomers freely diffuse. In a situation with high collision efficiencies (diffusion controlled association), higher levels of R will reduce association rates in general due to slower protein mobility, but this trend is weak for static organized R configurations.

Supporting Information. Simulations varying the number of active sites. Simulations of the tracks configuration varying the track mean length.

ACKNOWLEDGMENTS. We would like to thank Juan Manuel Pedraza for the motivation he provided at the initial stages of this work. This work was supported with funding from the Faculty of Sciences at Universidad de los Andes.

REFERENCES

- (1) Rieke, F.; Baylor, D.A. Single-photon detection by rod cells of the retina. *Rev. Mod. Phys.* 1998, 70, 1027-1036.
- (2) Cone, R.A. Rotational diffusion of rhodopsin in the visual receptor membrane. *Nat. New Biol.* 1972, 236, 39-43.
- (3) Poo, M.M.; Cone, R.A. Lateral diffusion of rhodopsin in the photoreceptor membrane. *Nature.* 1974, 247, 438-441.
- (4) Whited, A.M.; Park, P.S.H. Nanodomain organization of rhodopsin in native human and murine rod outer segment disc membranes. *Biochim. Biophys. Acta - Biomembr.* 2015, 1848, 26-34.
- (5) Liang, Y.; Fotiadis, D.; Filipek, S.; Saperstein, D.A.; Palczewski, K.; Engel, A. Organization of the G protein-coupled receptors rhodopsin and opsin in native membranes. *J. Biol. Chem.* 2003, 278, 21655-21662.
- (6) Suda, K; Filipek, S.; Palczewski, K.; Engel, A.; Fotiadis, D. The supramolecular structure of the GPCR rhodopsin in solution and native disc membranes. *Mol. Membr. Biol.* 2004, 21, 435-446.

face of trypanosomes. Like the trypanosome surface membrane, the vacuolar membrane had underlying microtubules (Fig. 5F). The origin of these structures is unknown, but it may involve membrane transport or targeting.

The toxicity of O-11 for bloodstream trypanosomes may be related to the metabolism or function of the VSG GPI, especially because similar concentrations do not affect the growth and viability of procyclic trypanosomes. However, our experiments cannot rule out the possibility that toxicity is mediated by alteration of N-myristoylated proteins or by some change in membrane structure. The latter could be caused by incorporation of analog into phospholipids as well as into VSG. Whatever the mechanism of toxicity, these studies suggest a new approach to antitrypanosome chemotherapy.

REFERENCES AND NOTES

- C. Laitman, *Trop. Dis. Res. News* 31, 3 (1990).
- S. L. Hajduk, P. T. Englund, D. H. Smith, in *Tropical and Geographic Medicine*, K. S. Warren and A. A. F. Mahmoud, Eds. (McGraw-Hill, New York, 1989), pp. 268–281; *Tropical Disease Research: Science at Work* (World Health Organization, Geneva, Switzerland, 1986).
- G. A. M. Cross, *Annu. Rev. Cell Biol.* 6, 1 (1990); T. L. Doering, W. J. Masterson, G. W. Hart, P. T. Englund, *J. Biol. Chem.* 265, 611 (1990); M. G. Low and A. R. Saltiel, *Science* 239, 268 (1988); J. R. Thomas, R. A. Dwick, T. W. Rademacher, *Biochemistry* 29, 5413 (1990).
- M. A. J. Ferguson and A. F. Williams, *Annu. Rev. Biochem.* 57, 285 (1988).
- M. A. J. Ferguson and G. A. M. Cross, *J. Biol. Chem.* 259, 3011 (1984).
- J. L. Krakow, D. Hereld, J. D. Bangs, G. W. Hart, P. T. Englund, *ibid.* 261, 12147 (1986).
- A. K. Menon, S. Mayor, M. A. J. Ferguson, M. Duszenko, G. A. M. Cross, *ibid.* 263, 1970 (1988).
- W. J. Masterson, T. L. Doering, G. W. Hart, P. T. Englund, *Cell* 56, 793 (1989).
- A. K. Menon, R. T. Schwarz, S. Mayor, G. A. M. Cross, *J. Biol. Chem.* 265, 9033 (1990).
- W. J. Masterson, J. Raper, T. L. Doering, G. W. Hart, P. T. Englund, *Cell* 62, 73 (1990).
- A. Mellors and A. Samad, *Parasitol. Today* 5, 239 (1989).
- H. Dixon, *Trans. R. Soc. Trop. Med. Hyg.* 61, 12 (1967); D. M. Raben, unpublished observations.
- R. O. Heuckeroth, L. Glaser, J. I. Gordon, *Proc. Natl. Acad. Sci. U.S.A.* 85, 8795 (1988).
- R. O. Heuckeroth and J. I. Gordon, *ibid.* 86, 5262 (1989).
- D. R. Johnson *et al.*, *ibid.* 87, 8511 (1990).
- J. L. Krakow, T. L. Doering, W. J. Masterson, G. W. Hart, P. T. Englund, *Mol. Biochem. Parasitol.* 36, 263 (1989); S. Mayor *et al.*, *J. Biol. Chem.* 265, 6164 (1990); S. Mayor, A. K. Menon, G. A. M. Cross, *ibid.*, p. 6174.
- T. L. Doering, L. U. Buxbaum, J. Raper, unpublished observations.
- The CoA derivative of O-11 (and of O-6 and O-13) is synthesized in the cell-free system as readily as that of myristate (17).
- Glycolipid A and its [³H]O-11-labeled counterpart are cleaved by PI-PLC from *Bacillus thuringiensis*, GPI-PLC from *T. brucei*, and GPI-PLD from human serum; glycolipid C and its counterpart only by GPI-PLD (PLC, phospholipase C; PLD, phospholipase D). Conditions were as in (8).
- All analogs and myristate were adjusted to the same specific radioactivity throughout.
- Mass analysis showed that after 6 hours of culture with 10 μM O-11 4% of the fatty acids on trypanosome VSG were O-11, affecting up to 8% of the VSG molecules (17).
- M. L. Bryant, R. O. Heuckeroth, J. T. Kimata, L. Ratner, J. I. Gordon, *Proc. Natl. Acad. Sci. U.S.A.* 86, 8655 (1989); M. L. Bryant *et al.*, *ibid.* 88, 2055 (1991).
- J. P. Richardson, R. P. Beecroft, D. L. Tolson, M. K. Liu, T. W. Pearson, *Mol. Biochem. Parasitol.* 31, 203 (1988); C. E. Clayton and M. R. Mowatt, *J. Biol. Chem.* 264, 15088 (1989).
- Lysate preparation, washes, and incubation buffers as in (10).
- J. D. Bangs, D. Hereld, J. L. Krakow, G. W. Hart, P. T. Englund, *Proc. Natl. Acad. Sci. U.S.A.* 82, 3207 (1985).
- T. L. Doering, W. J. Masterson, P. T. Englund, G. W. Hart, *J. Biol. Chem.* 264, 11168 (1989).
- Methanolysis of glycolipids A and C and examination of the resulting fatty acid methyl esters by reverse-phase thin layer chromatography showed that O-11 or myristate incorporated into these GPI species was not metabolized; similar analysis of the other (less polar) labeled lipids showed that they contained both unmodified [³H]O-11 or [³H]myristate as well as species that had been elongated (17).
- B. Hamm, A. Schindler, D. Mecke, M. Duszenko, *Mol. Biochem. Parasitol.* 40, 13 (1990).
- I. Cunningham, *J. Protozool.* 24 (no. 2), 325 (1977).
- G. A. M. Cross, *Parasitology* 71, 393 (1975).
- Supported by grants from the National Institutes of Health (AI21334 and AI27179), from the MacArthur Foundation, and from Monsanto Company. T.L.D. and L.U.B. are supported by Medical Scientist Training grant ST32GM07309. We are grateful to J. Welply (Monsanto Corporation) for suggesting this collaboration. We appreciate M. Delannoy's help with the electron microscopy and T. Ting's and I. Chu's assistance with phase microscopy. We thank V. Klein and S. Skiles for technical support; M. S. Pessin-Minsley and D. M. Raben for helpful advice; P. Talay, T. A. B. Shapiro, and K. Mensa-Wilmot for reviewing this manuscript; and J. D. Bangs and W. J. Masterson for discussions. We thank G. A. M. Cross for providing *T. brucei* strain 427 (variant 221). We thank J. Eid and C. Decker for providing trypanosome strain TREU 667.

25 January 1991; accepted 9 May 1991

Reading a Neural Code

WILLIAM BIALEK,* FRED RIEKE,* ROB R. DE RUYTER VAN STEVENINCK,† DAVID WARLAND

Traditional approaches to neural coding characterize the encoding of known stimuli in average neural responses. Organisms face nearly the opposite task—extracting information about an unknown time-dependent stimulus from short segments of a spike train. Here the neural code was characterized from the point of view of the organism, culminating in algorithms for real-time stimulus estimation based on a single example of the spike train. These methods were applied to an identified movement-sensitive neuron in the fly visual system. Such decoding experiments determined the effective noise level and fault tolerance of neural computation, and the structure of the decoding algorithms suggested a simple model for real-time analog signal processing with spiking neurons.

ALL OF AN ORGANISM'S INFORMATION about the sensory world comes from real-time observation of the activity of its own neurons. Incoming sensory information is represented in sequences of essentially identical action potentials, or "spikes." To understand real-time signal processing in biological systems, one must first understand this representation: Does a single neuron signal only discrete stimulus "features," or can the spike train represent a continuous, time-varying input? How much information is carried by the spike train? Is the reliability of the encoded signal limited by noise at the sensory input or by noise and inefficiencies in the subsequent layers of neural processing? Is the neural code robust to errors in spike timing? Clear experimental

answers to these questions have been elusive (1, 2). We present an approach to the characterization of the neural code that provides explicit and sometimes surprising answers to these questions.

The first recordings from single sensory neurons demonstrated that the intensity of a static stimulus can be coded in the firing rate of a sensory neuron (3). This concept of rate coding, extended to time-dependent stimuli, provides the framework for most studies of neural coding, leading to the definition of receptive fields, temporal filter characteristics, and so on. Beyond rate coding, a variety of different statistical measures have been proposed—interval distributions, correlation functions, and so forth (1, 4). As with the rate itself, these quantities can be seen as moments of the probability distribution $P\{\{t_i\}_i | s(\tau)\}$ that describes the likelihood of different spike trains $\{t_i\}$, given the stimulus $s(\tau)$ (5). These moments, however, are not properties of a single spike train; they are average properties of an ensemble of spike trains (6). Organisms rarely have the opportunity to compute these averages: To say that information is coded in firing rates is of no use to the organism unless one can

*Present address, NEC Research Institute, 4 Independence Way, Princeton, NJ 08540.
†Present address, Department of Audiology, University Hospital, P.O. Box 30.001, 9700 RB, Groningen, the Netherlands.

explain how the organism could estimate these firing rates from real-time observation of the spike trains of its own neurons (7).

The simplest problem of real-time signal processing is decoding the spike train to estimate the signal waveform. If one chooses an inappropriate definition of the signal this reconstruction will fail; for example, we have studied auditory neurons that provide enough information for reconstruction of the envelope of the acoustic stimulus but not of the waveform itself (8). One can define the signal encoded by a particular neuron to be that signal which is reconstructed most accurately from observation of the spike train. If one can reconstruct analog signals, then one can begin to understand how spike trains could be manipulated in subsequent stages of neural circuitry to perform more complex processing of these signals. It may not be possible, however, to interpolate between the discrete spikes to estimate a continuous stimulus.

The decoding problem is completely specified by the probability $P[s(\tau)|\{t_i\}]$ of a particular stimulus waveform $s(\tau)$ conditional on the spike train $\{t_i\}$. From this distribution, one can estimate the stimulus, for example, by finding the function of time that maximizes $P[s(\tau)|\{t_i\}]$. Thus, one approach to the decoding problem is to design experiments that directly measure $P[s(\tau)|\{t_i\}]$ (2). An alternative approach is to model the encoding process and analytically develop decoding algorithms within the context of the model; this approach (9) indicates that there is a broad regime in which linear filtering of the spike train results in an optimal estimate of the stimulus waveform (10). Are such simple decoding algorithms applicable to a real neuron?

The problem of reading the neural code is essentially the problem of building a (generally nonlinear) filter that operates continuously on the spike train to produce a real-time estimate of the unknown stimulus waveform (Fig. 1). If the spikes arrive at times $\{t_i\}$, our estimate of the signal is

$$s_{\text{est}}(t) = \sum_i F_1(t - t_i) + \sum_{i,j} F_2(t - t_i, t - t_j) + \dots \quad (1)$$

To optimize the reconstructions one chooses the filters $\{F_n\}$ to minimize $\chi^2 = \int dt |s(t) - s_{\text{est}}(t)|^2$, where $s(t)$ is the true stimulus and the integration is over the duration of the experiment (11). The stimulus $s(t)$ is not restricted to simple sine waves or Gaussian noise, and thus one can study the coding of complex and naturalistic signals (8, 12). In this initial experiment, however, we used relatively simple stimuli.

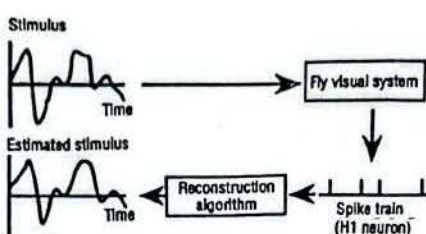


Fig. 1. Schematic view of the decoding process. The "black box" filters the spike train input $\{t_i\}$ to produce an estimate $s_{\text{est}}(\tau)$ of the stimulus.

We applied these ideas in experiments on a single, wide-field, movement-sensitive neuron (H1) in the visual system of the blowfly *Calliphora erythrocephala*. H1 encodes rigid horizontal movements over the entire visual field (13). Flies and other insects exhibit visually guided flight; during chasing behavior, course corrections can occur on time scales as short as 30 ms (14). The maximum firing rate in H1 is 100 to 200 s^{-1} , so behavioral decisions are based on just a few spikes from this neuron. Furthermore, the horizontal motion detection system consists of only a handful of cells, so the fly has no opportunity to compute average responses (for example, firing rates).

In our experiments, the stimulus $s(\tau)$ was the angular velocity of a rigidly moving random pattern. We chose $s(\tau)$ from an ensemble that approximated Gaussian noise with standard deviation 132 deg s^{-1} ; the spectrum of $s(\tau)$ was constant up to a cutoff frequency of 1 kHz. We recorded the spike arrival times $\{t_i\}$ extracellularly from the H1 neuron (2, 15). We began by trying to reconstruct $s(\tau)$ with just the linear term of the general expansion, Eq. 1 (Fig. 2). Reconstructions including higher order terms

in Eq. 1 were not significantly different, as quantified below. The filters used in the reconstruction integrated over short time intervals, so the optimal estimate of angular velocity at each instant of time was controlled by just a handful of spikes, as expected from behavioral studies.

How good are the reconstructions? The reconstructions consist of a piece that is deterministically related to the stimulus and a random noise piece. We separated these by introducing a frequency-dependent gain $g(\omega)$ such that $\tilde{s}_{\text{est}}(\omega) = g(\omega) [\tilde{s}(\omega) + \tilde{n}(\omega)]$, where $\tilde{n}(\omega)$ is the noise referred to the input. In a plot of $\tilde{s}(\omega)$ versus $\tilde{s}_{\text{est}}(\omega)$, the gain is the slope of the best linear fit and $\tilde{n}(\omega)$ is the scatter about this line. The distribution of $\tilde{n}(\omega)$ is approximately Gaussian.

Plotting the spectral density of the angular displacement noise, we found (Fig. 3) a peak signal-to-noise ratio (SNR) of better than 5:1, and an SNR of greater than one across a bandwidth of roughly 25 Hz. Using Shannon's formula (16), shown in Eq. 2, we converted these spectra into an estimate of the average rate at which we gained information about the stimulus (R_{info}) by virtue of observing the spike train; the result was 64 ± 1 bits per second (baud).

$$R_{\text{info}} = \int \frac{d\omega}{2\pi} \log_2 \left[1 + \frac{\langle |\tilde{s}(\omega)|^2 \rangle}{\langle |\tilde{n}(\omega)|^2 \rangle} \right] \quad (2)$$

The second term in the expansion improved the information rate by less than 5%. We have not explored conditions that might maximize this information transmission.

The noise level achieved in the reconstructions is the noise against which an observer of the H1 spike trains (such as the fly) must discriminate to estimate horizontal motion.

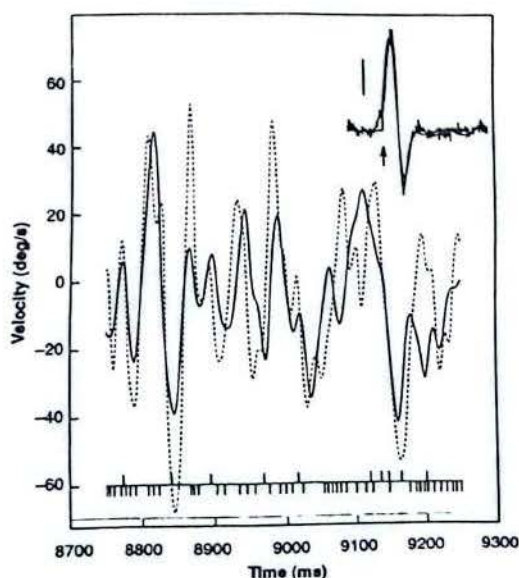


Fig. 2. First-order reconstruction (solid line) using method 1 (11). The stimulus is shown as a dotted line for comparison, and the spike train is shown at the bottom. This example is from a segment of the spike train that was not used in the filter calculations. Stimulus and reconstruction were smoothed with a 5-ms half-width Gaussian filter. (Inset) Filters calculated from methods 1 and 2 (11); the time scale is the same as the main figure, the scale bar = 10 deg s^{-1} , and the arrow marks $t = 0$. H1 has a highly asymmetric response profile, with a much larger dynamic range for movement in the excitatory direction. To compensate for this asymmetry, we recorded spike trains in response to $s(t)$ and to the inverted stimulus $-s(t)$; these are shown as positive and negative spikes in the spike train. These two spike trains approximate the trains that would be generated by H1 cells on opposite sides of the head during a rigid rotation of the fly (2). Our reconstruction is then

$$s_{\text{est}}(t) = \sum_i [F_1(t - t_i^+) - F_1(t - t_i^-)].$$

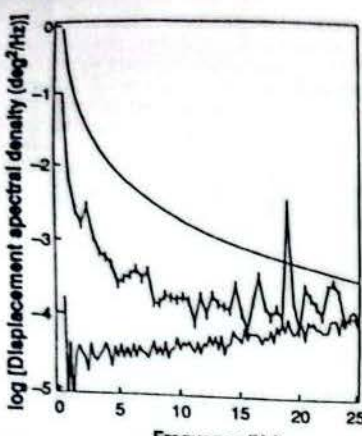


Fig. 3. Stimulus level (smooth curve) and spectral density of displacement noise from the reconstruction (middle curve). The bottom curve is the limit to the resolution of small displacements (valid for frequencies > 10 Hz) set by noise in the photoreceptor array (5).

$$S_{\text{eff}}(\omega) = \frac{S_v(\omega)}{|\tilde{T}(\omega)|^2} \frac{32\pi^{1/2}}{NS_c} \frac{(\Delta\phi)^5}{\phi_0^2}$$

$$\sinh[(1/2)(\phi_0/\Delta\phi)^2] \quad (4)$$

where S_v is the spectral density of the random contrast pattern used in the experiment, $\Delta\phi$ is the width of the photoreceptor aperture, ϕ_0 is the photoreceptor spacing along the direction of movement, $\tilde{T}(\omega)$ is the frequency response of the photoreceptor (millivolts per unit contrast), and $S_v(\omega)$ is the spectral density of voltage noise in the photoreceptor. The limiting noise power spectrum varies as the inverse of the number N of photoreceptors. These quantities were measured in photoreceptor recordings under conditions identical to those used for the H1 experiments (15), so we can make meaningful comparisons of theory and experiment.

The absolute noise level of the reconstructions is very low. With a behaviorally relevant integration time of 30 ms, one could judge the amplitude of a 20-Hz dither to within ~ 0.1 deg, which should be compared to the photoreceptor spacing of $\phi_0 = 1.35^\circ$. This angular resolution corresponds to the phenomenon of hyperacuity in human vision (17) and is in quantitative agreement with direct measures of discriminability for stepwise displacements in H1 (15). Defining an equivalent spectral density of noise in a spiking neuron allows one to exhibit hyperacuity in a real-time estimation task.

Information about movement across the visual field is carried in the spatiotemporal correlations of photoreceptor outputs, but these correlations are degraded by noise in the photoreceptors. How accurately can one estimate rigid motion if one optimally processes these noisy photoreceptor signals? In our stimulus ensemble, the angular displacements were small ($\delta\theta \ll \phi_0$) for frequencies above 10 Hz. In this limit, the optimal movement estimator involves multiplying the direct cur-

rent voltage in one cell by the alternating current voltage in its nearest neighbor (5). This is essentially the "correlation" scheme for movement detection proposed by Reichardt (18); in our case, this algorithm was not a minimal model but rather the optimal computational strategy. Analysis of the correlation scheme (5) led to the limiting angular displacement noise level shown in Fig. 3, where the displacement noise from the linear reconstruction approaches the limits imposed by the photoreceptor noise, at least at frequencies above 10 Hz, where our theory of the limiting noise level is valid. The fly visual system thus performs an optimal and nearly noiseless extraction of movement signals from the array of photoreceptor voltages.

Coding is often used to reduce the effects of noise on signal transmission. Does the neural code have any such noise immunity? For several noise sources, such as timing errors, dropped spikes, and spontaneously generated spikes, we created an ensemble of spike trains which were randomly corrupted versions of the original data and then treated these as new data that required decoding. We were able to recover 95% of the original information R_{info} for the following noise levels: (i) spikes added to increase the firing rate by 20%, (ii) 5% of the spikes deleted, and (iii) Gaussian timing jitter with standard deviation of 2 ms introduced to each spike time. One objection to "spike timing" as a coding strategy is the need for precise measurement of spike arrival times. In the case of H1, this objection is irrelevant. The code is robust to errors of several milliseconds in spike timing and to other corruptions of the spike train.

Preliminary results from four studies suggest that linear decoding is not a special property of H1 under particular stimulus conditions but a more general property of sensory neurons.

1) In H1, we performed reconstruction experiments using stimuli with different spatial characteristics. These different stimulus ensembles provided different SNRs, and these differences were reflected in the reconstructions. Despite large changes in SNR, linear reconstruction continued to work and the reconstruction filters were essentially identical up to a constant scale factor.

2) In the mechanoreceptor cells of the cricket cercal system, the displacement waveform for motions of the filiform hairs was reconstructed from the spike trains of primary afferent neurons (12). For this system, the information transfer rates exceeded 300 baud (~ 3 bits per spike).

3) In simulations on realistic models (19) for spike initiation, we reconstructed the waveform of injected currents by linearly filtering the spike train.

5
4) In vibratory receptors of the bullfrog saccus, we reconstructed the waveform of groundborne vibration using a linear decoding algorithm, although in this case the reconstructions improved substantially (by ~ 10 to 15%) with the addition of second-order terms (8). We again measured information rates close to 3 bits per spike.

It is, of course, not known if organisms perform the sort of reconstructions demonstrated in Fig. 2. Because linear reconstruction is possible, however, analog processing of the encoded signals can be done in a simple way. It is not unusual for the postsynaptic voltage response to a single presynaptic spike to have the qualitative form of the optimal filter, with a relatively sharp positive peak followed by a slower negative tail. Thus simple synapses could serve as decoders. With this decoding done, cells could then perform analog computations using the nonlinearities contributed by voltage-gated channels along the dendrites and cell body, much as envisioned for nonspiking cells (20). The results of such analog computations could then be encoded by the spike-generating region of the cell, and the process could then begin again. In this view of computation with spike trains, the combination of nonlinearities in spike generation and the filter characteristics of the synapse results in an essentially linear transmission of analog signals from presynaptic cell bodies to postsynaptic dendrites. The dramatic "all-or-none" nonlinearities of spike generation (the focus of so many models for neural computation) are then not as important as the more subtle analog dynamic properties of nonspiking regions of the cell.

It is surprising that time-dependent signals can be recovered so simply from neural spike trains. Reconstruction of the stimulus waveform permitted quantification of the fault tolerance of the code and allowed us to show that the fly visual system approaches optimal real-time computation. These results demonstrate that the representation of time-dependent sensory data in the nervous system is simpler than might have been expected. Correspondingly simpler models of sensory signal processing may be appropriate.

REFERENCES AND NOTES

- D. Perkel and T. Bullock, *Neurosci. Res. Program Bull.*, **6**, 221 (1968).
- R. R. de Ruyter van Steveninck and W. Bialek, *Proc. R. Soc. London Ser. B* **234**, 379 (1988).
- E. D. Adrian, *J. Physiol.* **61**, 47 (1926).
- Recent work has focused attention on the time variation of firing rates in the auditory [for example, M. I. Miller, P. E. Bartaand, M. B. Sachs, *J. Acoust. Soc. Am.* **81**, 665 (1987)] and visual [for example, B. J. Richmond, L. M. Optican, H. Spitzer, *J. Neurophysiol.* **64**, 351 (1990)] systems and on the